Published in "Developmental Cell 46 (2): 145-161.e10, 2018"
which should be cited to refer to this work.

Nrf2-Mediated Fibroblast Reprogramming Drives Cellular Senescence by Targeting the Matrisome

Paul Hiebert,[1,*] Mateusz S. Wietecha,[1] Michael Cangkrama,[1] Eric Haertel,[1] Eleni Mavrogonatou,[2] Michael Stumpe,[3] Heiko Steenbock,[4] Serena Grossi,[5] Hans-Dietmar Beer,[5] Peter Angel,[6] Jürgen Brinckmann,[4,7] Dimitris Kletsas,[2] Jörn Dengjel,[3] and Sabine Werner[1,8,*]

[1]Institute of Molecular Health Sciences, Department of Biology, Swiss Federal Institute of Technology (ETH) Zurich, Otto-Stern-Weg 7, 8093 Zurich, Switzerland
[2]Laboratory of Cell Proliferation and Ageing, Institute of Biosciences and Applications, National Centre for Scientific Research "Demokritos", Athens, Greece
[3]Department of Biology, University of Fribourg, 1700 Fribourg, Switzerland
[4]Institute of Virology and Cell Biology, University of Lübeck, 23562 Lübeck, Germany
[5]Faculty of Medicine, University of Zürich, 8091 Zürich, Switzerland
[6]Division of Signal Transduction and Growth Control, German Cancer Research Center (DKFZ), Heidelberg, Germany
[7]Department of Dermatology, University of Lübeck, 23538 Lübeck, Germany
[8]Lead Contact
*Correspondence: paul.hiebert@biol.ethz.ch (P.H.), sabine.werner@biol.ethz.ch (S.W.)

SUMMARY

Nrf2 is a key regulator of the antioxidant defense system, and pharmacological Nrf2 activation is a promising strategy for cancer prevention and promotion of tissue repair. Here we show, however, that activation of Nrf2 in fibroblasts induces cellular senescence. Using a combination of transcriptomics, matrix proteomics, chromatin immunoprecipitation and bioinformatics we demonstrate that fibroblasts with activated Nrf2 deposit a senescence-promoting matrix, with plasminogen activator inhibitor-1 being a key inducer of the senescence program. *In vivo*, activation of Nrf2 in fibroblasts promoted re-epithelialization of skin wounds, but also skin tumorigenesis. The pro-tumorigenic activity is of general relevance, since Nrf2 activation in skin fibroblasts induced the expression of genes characteristic for cancer-associated fibroblasts from different mouse and human tumors. Therefore, activated Nrf2 qualifies as a marker of the cancer-associated fibroblast phenotype. These data highlight the bright and the dark sides of Nrf2 and the need for time-controlled activation of this transcription factor.

INTRODUCTION

Many strategies for promotion of tissue repair and protection from cancer and various inflammatory diseases are aimed at reducing the impact of harmful reactive oxygen species (ROS) on susceptible cells (Wondrak, 2009). Central to this effort has been the use of pharmaceuticals targeting the activation of the transcription factor nuclear factor-erythroid 2-related factor 2 (NRF2; NFE2L2). Considered as a "master regulator of the antioxidant response," NRF2 controls the transcription of genes encoding ROS-detoxifying enzymes and various other antioxidant proteins (Kansanen et al., 2013; Sykiotis and Bohmann, 2010; Taguchi et al., 2011). During cellular homeostasis, NRF2 is mainly located in the cytoplasm via interaction with Kelch-like ECH-associated protein 1 (KEAP1), followed by its rapid ubiquitination and proteasomal degradation. Activation of NRF2 occurs through electrophile-induced conformational changes of KEAP1, resulting in weakening of the NRF2-KEAP1 interaction. Furthermore, ROS activate certain kinases that phosphorylate NRF2, thereby affecting KEAP1 binding. As a consequence, newly synthetized NRF2 is stabilized, accumulates in the nucleus, and together with small Maf proteins binds to specific sites of the DNA called antioxidant response elements (AREs) in the promoters or enhancers of its target genes (Suzuki and Yamamoto, 2017; Sykiotis and Bohmann, 2010). Therefore, NRF2 activating compounds protect from oxidative stress, and preclinical and first clinical studies showed positive effects in cancer prevention and in the treatment of inflammatory and neurodegenerative diseases (Liby and Sporn, 2012; Sporn and Liby, 2012).

As the outermost surface of our body, the skin is frequently exposed to various challenges that induce the production of harmful ROS. Accordingly, skin cells are well equipped with a variety of antioxidant defense mechanisms in which NRF2 plays a central role (Schäfer and Werner, 2008). For example, Nrf2 activating compounds protected mice from UV-induced cell damage and carcinogenesis and promoted wound repair in diabetic mice (Long et al., 2016; Talalay et al., 2007). Since these compounds also have Nrf2-independent activities and affect all cell types, we previously used a genetic approach to specifically activate Nrf2 in a cell-type-specific manner using transgenic mice expressing a truncated form of Nrf2 that lacks the Keap1 binding domain and thus acts as a constitutively active Nrf2 (caNrf2) mutant (Schäfer et al., 2010, 2014; Schäfer et al., 2012). The caNrf2 model has been well characterized both *in vitro* and *in vivo* as a means of specifically activating Nrf2

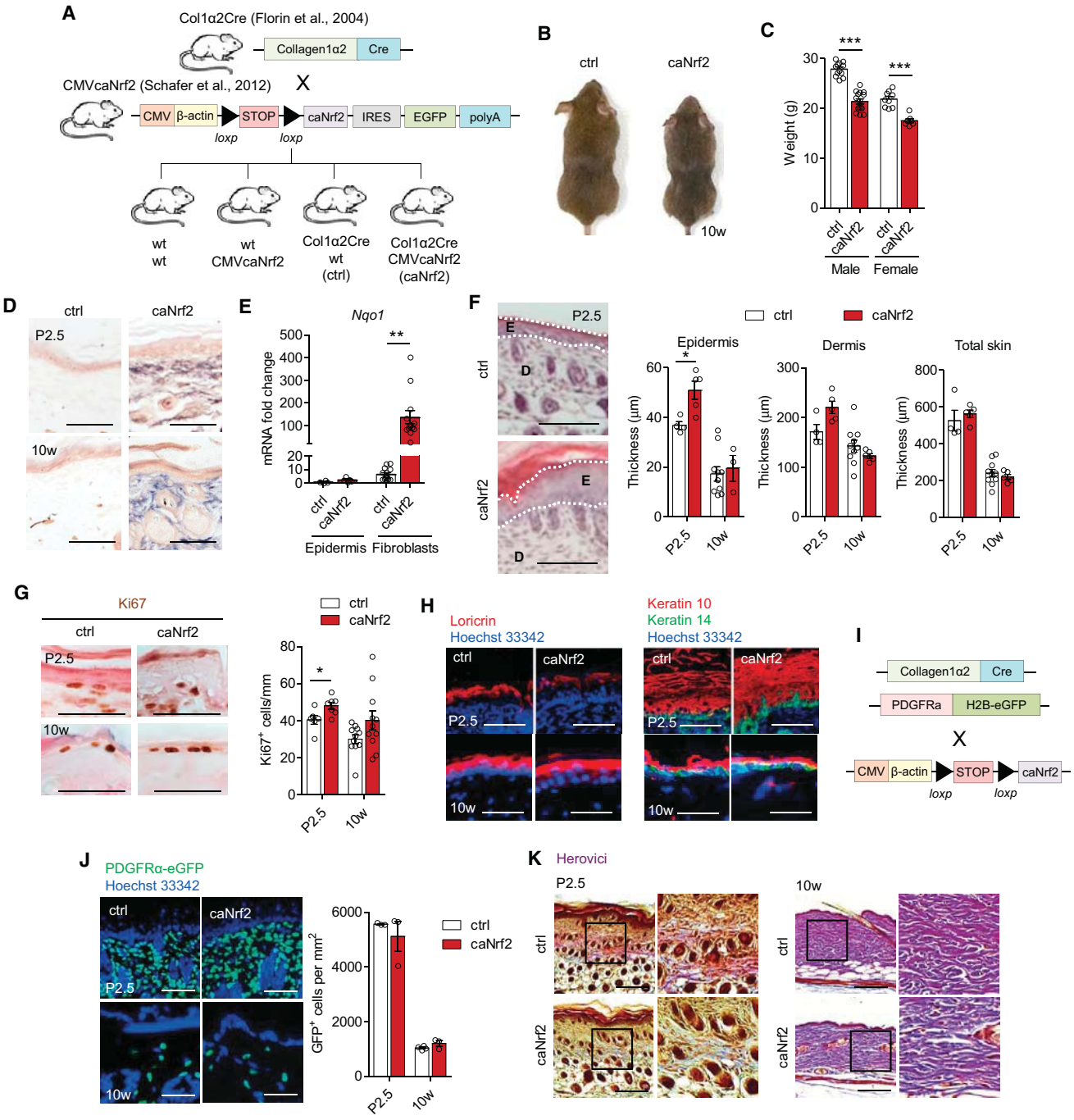

Figure 1. Nrf2 Activation in Fibroblasts Controls Keratinocyte Proliferation and Collagen Production in Mice

(A) Schematic representation of the constructs used for the generation of transgenic mice and breeding scheme for the generation of mice expressing caNrf2 in fibroblasts.

(B) Macroscopic appearance of ctrl and caNrf2 mice at 10 weeks of age.

(C) Body weight of caNrf2 mice at 10 weeks of age (N = 7–15 animals).

(D) hPAP staining of skin from ARE-hPAP/ctrl and ARE-hPAP/caNrf2 mice at post-natal day 2.5 (P2.5) and 10 weeks. Purple staining denotes Nrf2 activation.

(E) Relative gene expression (qRT-PCR) of the Nrf2 target gene *Nqo1* in epidermis tissue (N = 4–5) versus fibroblasts (N = 13–16).

(F) Skin histology and thickness at P2.5 (N = 4–5) and 10 weeks (N = 3–10) of age.

(G) Ki67 staining on skin from mice at P2.5 (N = 6–7) and 10 weeks of age (N = 7–8).

(H) Examination of keratinocyte differentiation using immunofluorescence for the differentiation-specific proteins keratin 10, keratin 14, and loricrin. Nuclei were counterstained with Hoechst 33342.

(I) Scheme describing the generation of triple transgenic mice containing the *PDGFRα-eGFP* transgene.

(legend continued on next page)

pathways at a level consistent with pharmacological activators of endogenous Nrf2 (Kohler et al., 2014; Schäfer et al., 2012; Schäfer et al., 2014). We used this model instead of a *Keap1* knockout, since Keap1 also targets other proteins besides Nrf2 (Lee et al., 2009; Mulvaney et al., 2016; Orthwein et al., 2015) and since dose-dependent effects of Nrf2 activation can be studied with the caNrf2 mutant.

Expression of caNrf2 in keratinocytes of transgenic mice indeed protected from oxidative stress caused by UV irradiation (Schäfer et al., 2010), but also had undesirable effects, such as hyperkeratosis, sebaceous gland hyperplasia and increased cancer cell survival (Rolfs et al., 2015; Schäfer et al., 2014). Surprisingly, there is little known regarding the consequences of Nrf2 activation in skin fibroblasts, representing a significant gap in our knowledge given the importance of stromal cells in mediating tissue repair and cancer.

Here we describe an Nrf2-mediated pathway in fibroblasts that leads to the onset of cellular senescence and a cancer-associated fibroblast (CAF) phenotype. We show that Nrf2 activation serves to reprogram fibroblasts via direct targeting of certain extracellular matrix (ECM) genes to trigger the onset of cellular senescence, leading to increased proliferation of keratinocytes and accelerated wound repair, but also enhanced skin tumorigenesis.

RESULTS

Fibroblast-Derived Nrf2 during Skin Homeostasis and Development

To study the role of Nrf2 in fibroblasts during skin homeostasis, repair and cancer we generated gain- and loss-of-function mouse models. Mice with floxed *Nfe2l2* alleles (Reddy et al., 2011) were crossed with Col1α2Cre mice (Florin et al., 2004), resulting in the generation of mice lacking a functional Nrf2 protein in mesenchymal cells, including dermal fibroblasts (designated ko, Figure S1A). Constitutive Nrf2 activation in fibroblasts was achieved by Cre-mediated deletion of a transcription/translation STOP cassette in front of the *caNrf2* transgene (Schäfer et al., 2012) using Col1α2Cre mice. The Col1α2Cre-caNrf2 double transgenic progeny (caNrf2 mice) express caNrf2 in mesenchymal cells (Figure 1A). Ko mice had no abnormalities in appearance or weight (Figure S1B). caNrf2 mice grew to adulthood without obvious differences in appearance compared with control (ctrl) mice with the exception of slightly reduced body size and weight (Figures 1B and 1C). The latter may result at least in part from the activity of the Col1α2Cre promoter in mesenchymal cells of other organs (Florin et al., 2004). Mating of the caNrf2 mice with mice expressing human placental alkaline phosphatase (hPAP) under control of the rat *NQO1* ARE and a minimal promoter (ARE-hPAP reporter mice), which allow for visualization of cells featuring Nrf2 activation (Johnson et al., 2002), demonstrated dermis-specific staining in the skin of triple transgenic progeny (Figure 1D). Importantly, there was no staining in keratinocytes, and expression of the classical Nrf2 target gene NAD(P)H dehydrogenase quinone 1 (*Nqo1*) was strongly induced by caNrf2 in fibroblasts, but not in the epidermis (Figure 1E).

The skin of caNrf2 mice was morphologically indistinguishable from control mice at 10 weeks of age. However, the epidermis was significantly thicker at post-natal day 2.5 (P2.5) (Figure 1F). This corresponded to increased proliferation of epidermal cells (Figure 1G). Examination of immune cell content in the skin by flow cytometry showed slightly elevated levels of neutrophils and natural killer cells, which may contribute to the increased proliferation observed in caNrf2 epidermis (Figure S1C). Keratinocyte differentiation was not affected (Figure 1H).

To visualize fibroblasts, we mated the caNrf2 mice with transgenic mice expressing EGFP under control of the platelet-derived growth factor receptor alpha (PDGFRα) gene promoter (Hamilton et al., 2003) (Figure 1I). The number of GFP-positive cells in the skin of caNrf2-positive triple mutant mice was similar to ctrl mice at P2.5 and 10 weeks (Figure 1J). Ki67 staining showed virtually no detectable proliferating GFP$^+$ cells (Figure S1D). Herovici staining, which stains collagen fibers blue/purple (Herovici, 1963), revealed a slight reduction in collagen at P2.5 in caNrf2 mice (Figure 1K).

Constitutive Activation of Nrf2 Promotes Fibroblast Senescence

To examine fibroblast behavior *in vitro*, fibroblasts were isolated from mouse skin at P2.5 and grown in culture. Flow cytometry analysis as well as expression analysis of cell-type-specific genes revealed virtual absence of endothelial and immune cells in the primary cultures (Figures S1E–S1H). A few keratinocytes were still present, but they are rapidly lost upon passaging due to their differentiation in medium with high calcium content.

Cultured caNrf2 skin fibroblasts showed a strong increase in the expression of classical Nrf2 target genes compared with ctrl fibroblasts (Figure 2A). Nrf2 activating compounds such as tert-butylhydroquinone (tBHQ), sulforaphane (SFN), and 2-cyano-3,12-dioxooleana-1,9-dien-28-imidazolide also upregulated Nrf2 target genes (e.g., *Nqo1*) to varying degrees, yet comparable with caNrf2-expressing fibroblasts (Figure S1I). This confirms the physiological relevance of caNrf2-expressing fibroblasts as a model of Nrf2 activation in this cell type. Skin fibroblasts from ko mice showed reduced expression of *Nqo1*, which failed to increase after treatment with Nrf2 activating compounds (Figure S1J).

Immunostaining demonstrated nuclear localization of Nrf2 in caNrf2 fibroblasts and also revealed a noticeable smaller cell size (Figure 2B). Surprisingly, caNrf2 fibroblasts showed a marked reduction in proliferation already by the second passage (Figures 2C and 2D), which correlated with increased mRNA levels of cell-cycle arrest genes commonly associated with cellular senescence (*p15ink4b, p16ink4a, p21Cip1*) (Figure 2E). Moreover, senescence-associated β-galactosidase (SA-β-gal)

(J) Skin sections from mice containing a PDGFRα-eGFP transgene for visualization of fibroblasts (green) and quantification of GFP-positive cells at P2.5 (N = 3) and 10 weeks of age (N = 4).

(K) Herovici staining of skin from mice at P2.5 and 10 weeks of age.

***p < 0.001, **p < 0.01, *p < 0.05, Mann-Whitney U test. Bar graphs show mean and SEM. Scale bars, 100 μm. See also Figure S1.

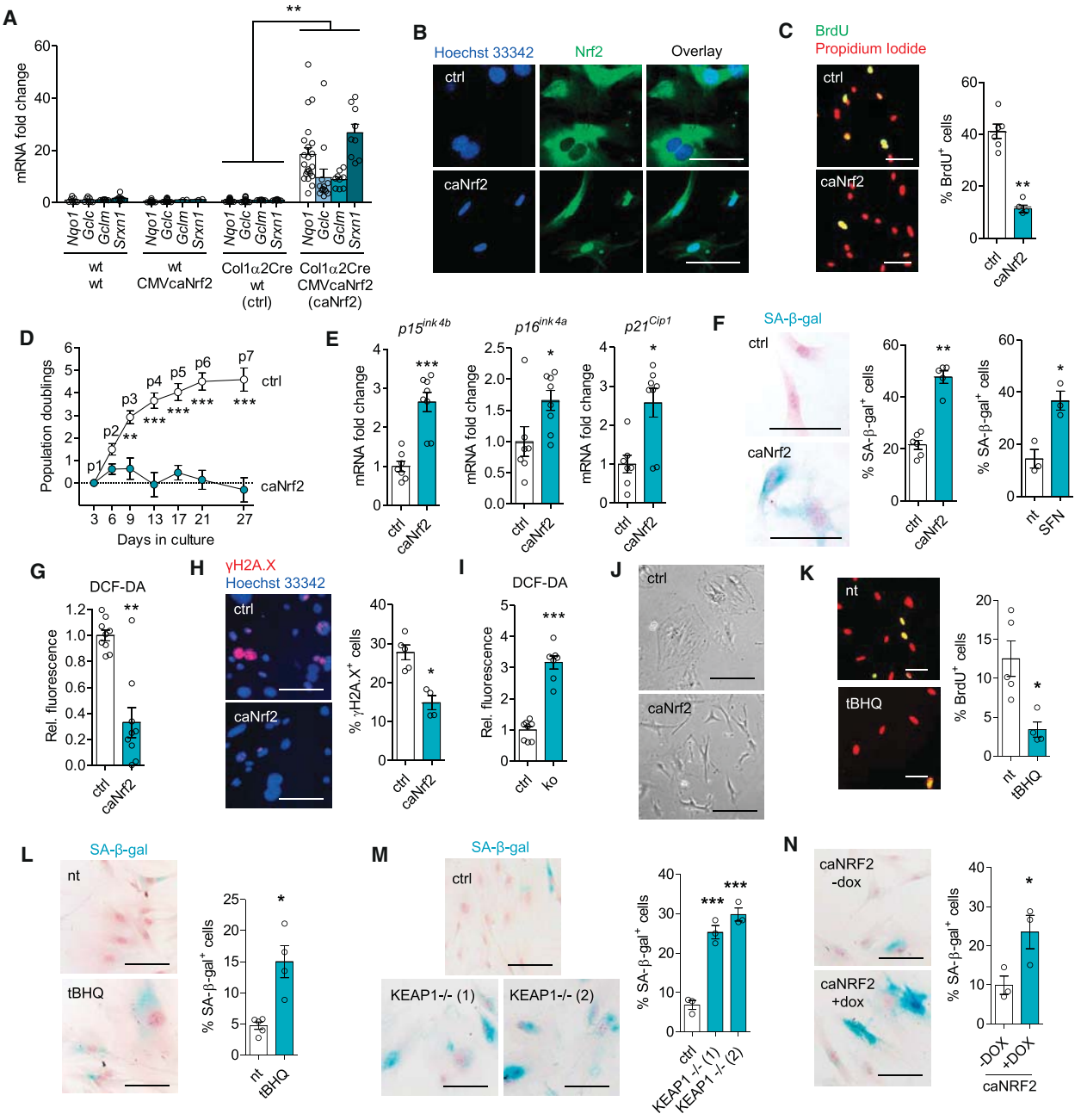

Figure 2. Constitutive Nrf2 Activation in Fibroblasts Promotes Cellular Senescence

(A–J) Fibroblasts were isolated from the skin of mice at P2.5 and analyzed at passage 2. (A) qRT-PCR analysis of Nrf2 target genes using RNA from primary fibroblasts isolated from mice at P1.5 (N = 9–22 cultures from different mice). (B) Immunofluorescence staining for Nrf2 (green) and counterstaining with Hoechst 33342 (blue) on fibroblasts from ctrl and caNrf2 mice. (C) 5-Bromo-2′-deoxyuridine (BrdU) labeling and immunofluorescence staining of fibroblasts (green) and counterstaining of nuclei with propidium iodide (red) (N = 4–6). (D) Population doublings of fibroblasts grown for seven passages by counting trypan blue excluding cells (N = 4–6). (E) Analysis of gene expression of the senescence markers *p15ink4b*, *p16ink4a*, and *p21Cip1* by qRT-PCR in fibroblasts (N = 7–8). (F) Fibroblasts from ctrl versus caNrf2 mice (N = 5–6) or from wild-type fibroblasts treated with SFN (N = 3) stained for SA-β-gal. (G) ROS detection by DCF-DA in fibroblasts from ctrl and caNrf2 mice (N = 8–9). (H) Immunofluorescence staining for γH2A.X to detect DNA damage (N = 4–5). (I) ROS detection by DCF-DA in fibroblasts from ctrl and ko (N = 7–8) mice. (J) Bright-field images of fibroblasts cultured from ctrl and caNrf2 mice.

(K and L) Human primary foreskin fibroblasts treated with tBHQ (n = 4–5 technical replicates) stained for BrdU (K) or SA-β-gal (L) at passage 15.

(M) Human primary fibroblasts transduced with a lentivirus allowing CRISPR/Cas9-mediated *KEAP1* knockout using two different single guide RNAs or control virus (n = 3) stained for SA-β-gal at passage 19.

(N) Human primary fibroblasts transduced with a lentivirus allowing doxycycline-inducible expression of caNRF2, treated with doxycycline or vehicle and stained for SA-β-gal at passage 19.

***p < 0.001, **p < 0.01, *p < 0.05, Mann-Whitney U test or student's t-test. Bar graphs show mean and SEM. Scale bars, 50 μm. See also Figure S1.

A

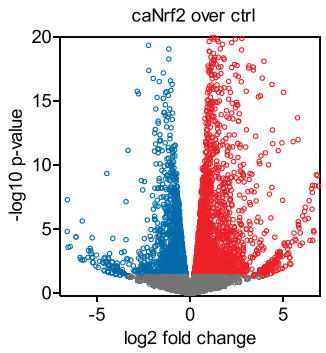

B

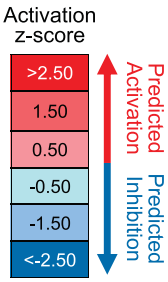

Selected Annotated Functions:	Activation z-score
Proliferation of cells	2.727
Proliferation of epithelial cells	1.755
Proliferation of fibroblast cell lines	-0.987
Apoptosis	-1.585
Migration of cells	4.340
Organization of cytoskeleton	1.765
Angiogenesis	2.637
Fibrogenesis	2.499

Input: 4574 genes (p-value < 0.05)
All functions -log$_{10}$(p-value) > 10

C

Upstream Regulator	Activation z-score
NFE2L2	**7.320**
1,2-dithiol-3-thione	6.525
phorbol myristate acetate	6.170
EGF	6.146
IL1	6.071
MYOCD	5.721
PDGF BB	5.658
TNF	5.421
CREB1	5.409
forskolin	5.264

D

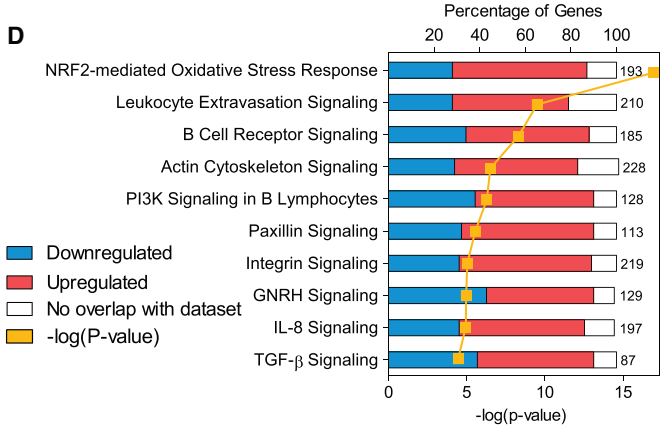

E

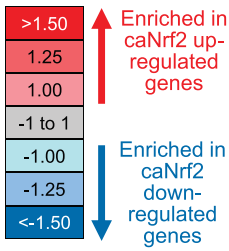

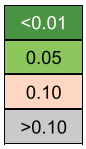

Fibroblast senescence associated gene sets:		caNrf2 *vs* ctrl fibroblasts NES	FDR
Bleomycin-treated *vs* young fibroblasts Top 348 genes	**UP**	1.68	0.000
Bleomycin-treated *vs* young fibroblasts Bottom 378 genes	**DOWN**	-1.76	0.000
Replicative senescent *vs* young fibroblasts Top 337 genes	**UP**	1.39	0.017
Replicative senescent *vs* young fibroblasts Bottom 267 genes	**DOWN**	-1.34	0.021

F

Senescence Associated Secretory Phenotype (SASP)

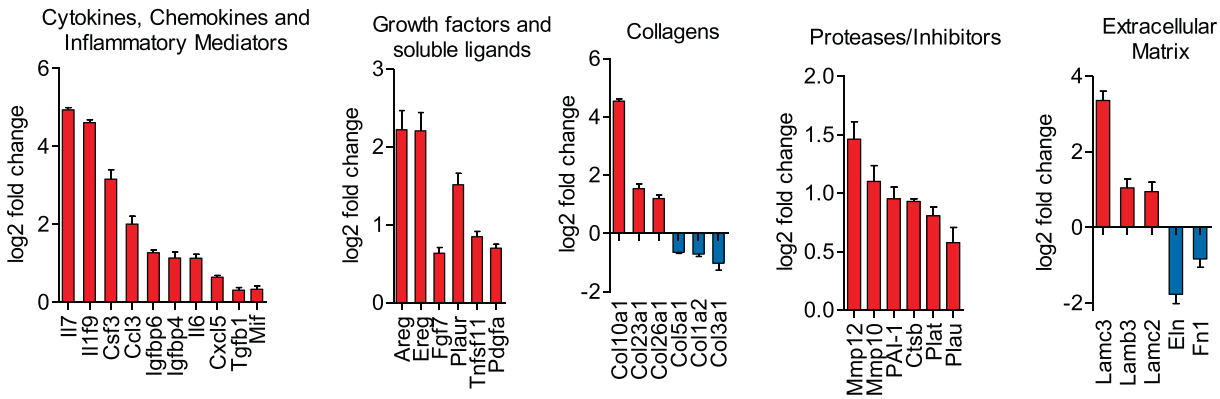

(legend on next page)

staining confirmed accelerated cellular senescence of caNrf2 fibroblasts (Figure 2F). Chronic treatment of wild-type fibroblasts with SFN also promoted senescence to a similar extent as the *caNrf2* transgene (Figure 2F). This was unexpected, since ROS detoxification is typically considered as protective against DNA damage and the subsequent onset of senescence (Macip et al., 2002; Qin et al., 2012; Weyemi et al., 2012). Examination of intracellular ROS levels using two separate ROS-detecting reagents confirmed that ROS levels are indeed reduced in caNrf2 fibroblasts (Figures 2G and S1K). caNrf2 fibroblasts also displayed reduced DNA damage shown by staining for γH2A.X (Figure 2H). As expected, ko fibroblasts had elevated ROS levels (Figure 2I), however showed no difference in proliferation or expression of senescence markers when examined at the same time and passage (Figures S1L and S1M). Furthermore, Nrf2-mediated senescence is not accompanied by cellular hypertrophy characteristic for senescent fibroblasts, since caNrf2 fibroblasts appeared smaller and spindle shaped (Figures 2B and 2J). These findings suggest that increased ROS levels and subsequent DNA damage are not responsible for Nrf2-mediated senescence and that activated Nrf2 induces senescence through an alternative pathway.

To see if Nrf2 activation also promotes senescence in human fibroblasts, we treated primary human foreskin fibroblasts with tBHQ every 3 days for 2 weeks. Indeed, this resulted in upregulation of *NQQ1* expression and a concomitant significant decrease in proliferation and increase in the percentage of senescent cells (Figures S1N, 2K, and 2L). Similar results were obtained when constitutive Nrf2 activation was achieved by transducing human fibroblasts with lentiviral constructs encoding a doxycycline-inducible caNRF2 mutant or upon CRISPR/Cas9-mediated knockout of *KEAP1* using two different single guide RNAs (Figures S1N, 2M, and 2N).

caNrf2 Fibroblasts Display a Senescence-Associated Gene Expression Pattern

To further determine if caNrf2 fibroblasts are indeed senescent, we performed RNA sequencing (RNA-seq) and found major changes in gene expression by caNrf2 compared with ctrl fibroblasts (Figure 3A). Ingenuity Pathway Analysis (IPA) predicted activation of epithelial cell proliferation, cell movement, cytoskeletal remodeling, angiogenesis, and fibrosis (Figure 3B; Table S1). By contrast, there was a predicted suppression of fibroblast proliferation and of apoptosis. Expectedly, the top upstream regulator predicted by IPA was Nrf2 (Figure 3C), while the top enriched and activated IPA canonical pathway was the "NRF2-mediated oxidative stress response" (Figure 3D; Table S1). Gene set enrichment analysis showed highly significant enrichment of both up- and downregulated genes in caNrf2 fibroblasts with genes affected by replicative or bleomycin-induced senescence in fibroblasts (Figure 3E; Table S2). caNrf2 fibroblasts also displayed a gene expression profile that featured genes commonly known as part of the "senescence-associated secretory phenotype" (SASP) that is characterized by expression of a variety of cytokines, growth factors and ECM proteins that strongly affect different types of neighboring cells (Coppe et al., 2010) (Figure 3F). This confirms that despite having reduced ROS levels and a smaller cell size, caNrf2 fibroblasts exhibit the classical functional characteristics of senescent cells.

Nrf2-Mediated Fibroblast Senescence Corresponds to Faster Re-epithelialization and Accelerated Wound Closure

To investigate the *in vivo* relevance of the fibroblast phenotype, we analyzed the healing process of full-thickness excisional wounds at 5 and 14 days post-wounding. By day 5, only a small percentage (22%) of wounds in ctrl mice had closed, while the majority (64%) of wounds in caNrf2 mice were closed at the same time point along with an overall increase in re-epithelialization (Figures 4A and 4B). At day 14, wounds from caNrf2 mice displayed reduced granulation/early scar tissue (Figures 4A, second panel, and 4C), however showed no observable difference in wound contraction at day 5 or 14 (Figures 4B and 4C). Immunofluorescence staining for α smooth muscle actin in 5-day wounds also showed no obvious difference in the amount or morphology of myofibroblasts (Figure 4A). Five-day wounds from caNrf2 mice did, however, exhibit a significant increase in SA-β-gal-positive cells in the granulation tissue at day 5 (Figures 4A and 4D). Interestingly, SA-β-gal-positive cells were not readily observed in unwounded dermis, suggesting that additional growth stimuli are required for Nrf2-mediated senescence. Consistent with this hypothesis, senescent cells were still present, but reduced by day 14, with no clear differences between genotypes (Figure S2A). Analysis of fibroblast proliferation using triple transgenic caNrf2-PDGFRα-eGFP mice and their caNrf2-negative controls also showed reduced Ki67-positive fibroblasts in the granulation tissue of caNrf2-positive mice at day 5 (Figures 4A and 4E). By contrast, keratinocyte proliferation was increased in the neo-epidermis of caNrf2 mice (Figures 4A and 4F), suggesting that caNrf2 fibroblasts stimulate keratinocyte proliferation, possibly through the secretion of keratinocyte mitogens. Consistent with this hypothesis, conditioned medium from caNrf2 fibroblasts promoted proliferation of cultured primary keratinocytes compared with conditioned medium from control cells (Figure 4G). Since the Col1α2Cre mouse also targets mesenchymal cells in blood vessel walls (Florin et al., 2004) (Figure S2B), we determined if wound angiogenesis is affected in the caNrf2-transgenic mice. However, the area of granulation tissue

Figure 3. caNrf2 Fibroblasts Display a Senescence-Associated Gene Expression Pattern

(A) Volcano plot showing differentially regulated genes identified in RNA-seq analysis of ctrl versus caNrf2 fibroblasts (N = 3 cultures per genotype from different mice).

(B–D) Ingenuity pathway analysis of differentially regulated genes in caNrf2 versus ctrl fibroblasts, showing selected top activated functions (B), top upstream regulators (C), and the top 10 canonical pathways (D) identified as enriched in caNrf2 fibroblasts.

(E) Gene set enrichment analysis comparing differentially regulated genes identified in caNrf2 fibroblasts with published datasets from fibroblasts undergoing bleomycin-induced senescence or replicative senescence.

(F) Differentially regulated genes in caNrf2 fibroblasts that correlate with genes previously observed to be disregulated as part of the SASP.

Bar graphs show mean and SEM. See also Tables S1 and S2.

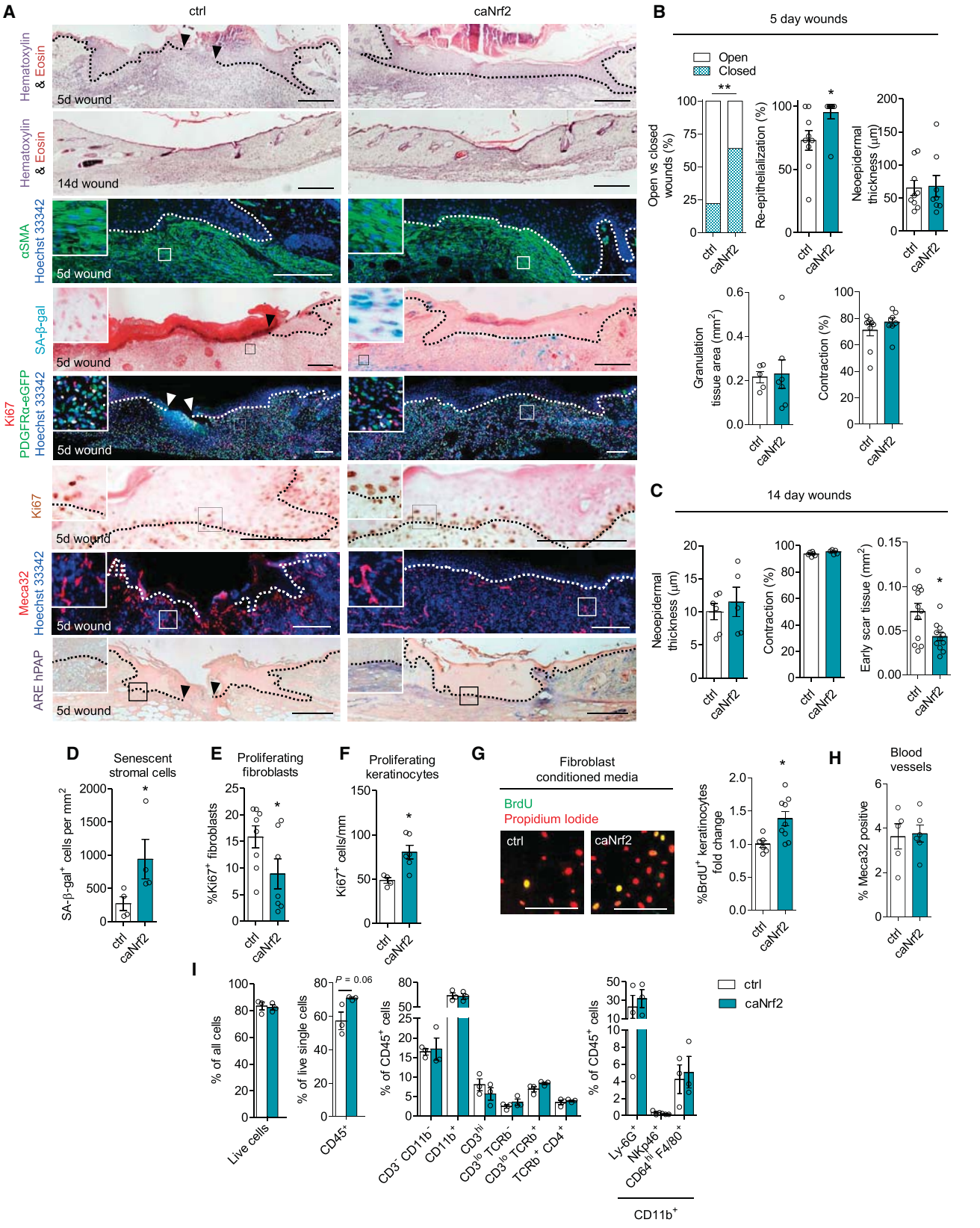

(legend on next page)

that stained positive for Meca32 was similar in both groups at day 5 (Figures 4A and 4H).

As cellular senescence is thought to increase with age, we also investigated wound healing in young (4-week-old) caNrf2 mice. Interestingly, SA-β-gal staining in wounds from young mice appeared even stronger than in adult mice, and this was particularly pronounced in the caNrf2 mutant mice (Figure S2C). Consistent with this early induction of the senescence program in wound fibroblasts, young ctrl and caNrf2 mice healed faster and showed complete closure of all wounds at day 5 (Figures S2D and S2E).

caNrf2-ARE-hPAP reporter mice showed caNrf2 expression throughout the dermis/granulation tissue, suggesting that senescence is occurring only in a subset of caNrf2-positive cells (Figure 4A). Immune cells and keratinocytes isolated from wounds of caNrf2 mice by fluorescence-activated cell sorting showed no increase in the expression of Nrf2 target genes (Figure S2F). No differences were observed in ko mice in either rates of wound closure or wound morphometry (Figures S2G–S2J). Together, these results demonstrate that Nrf2 in fibroblasts is dispensable for normal wound healing, but that persistent activation of Nrf2 promotes fibroblast senescence *in vivo* and results in increased keratinocyte proliferation and faster re-epithelialization.

Analysis of immune cell content by flow cytometry showed a slight increase in immune cells ($CD45^+$) in unwounded skin from caNrf2 mice, however, there was no significant difference in frequencies for any of the immune cell subtypes examined in 5-day wounds (Figures 4I and S3A). Ko mice showed mild increases in the frequencies of T cells ($CD3^{hi}$, $CD3^{lo}/TCR\beta^-$, or $TCR\beta^+$) and natural killer cells ($CD11b^+/NKp46^+$) in unwounded skin, while the frequency of macrophages ($CD11b^+/CD64^{hi}/F4/80^+$) was increased. These differences were, however, not observed in 5-day wounds (Figures S3B and S3C).

Overall, these results suggest that immune cells have little to no effect on the wound healing phenotype of caNrf2 mice and provide further evidence for a direct effect of senescent fibroblasts on keratinocyte proliferation.

Nrf2-Mediated Fibroblast Senescence Leads to a CAF Phenotype

Senescent fibroblasts expressing a SASP can promote cancer development and progression by behaving as CAFs (Bavik et al., 2006; Krtolica et al., 2001; Laberge et al., 2012; Liu and Hornsby, 2007; Parrinello et al., 2005; Procopio et al., 2015). Expression of several typical CAF markers was indeed elevated in caNrf2 fibroblasts compared with ctrl cells (Figure 5A), and differentially regulated genes in caNrf2 fibroblasts were enriched significantly with those upregulated in published datasets from mouse and human CAFs (Table S2; Figure 5B). Consistent with this finding, data of the Human Protein Atlas (Uhlen et al., 2015, 2017) (www.proteinatlas.org) demonstrate strong nuclear NRF2 staining of stromal cells in a variety of human cancers, including epithelial skin cancers (Figures S4A and S4B). Interestingly, upregulated genes in fibroblasts undergoing replicative or bleomycin-induced senescence (Pazolli et al., 2009) also showed enrichment with genes upregulated in CAFs, supporting a general link between fibroblast senescence and CAF activation (Figure 5B). Further analysis also demonstrated a link between Nrf2 activation and senescence in fibroblasts, as many enriched genes in senescence datasets corresponded to genes involved in the Nrf2 pathway and to those identified in Nrf2 chromatin immunoprecipitation sequencing (ChIP-seq) experiments (Malhotra et al., 2010) (Figure 5B).

To test the functional relevance of these findings, we mixed fibroblasts from ctrl or caNrf2 mice with weakly malignant human squamous cell carcinoma cells (SCC13 cell line [Rheinwald and Beckett, 1981]) and injected them either into the ear or the back skin of immunocompromised mice. Cells injected into back skin all developed tumors; however, tumors formed in the presence of caNrf2 fibroblasts were significantly larger and grew more invasively compared with those formed in the presence of ctrl fibroblasts (Figures 5C and 5D). While tumors failed to develop in the ear skin by 5 weeks when ctrl fibroblasts were used, caNrf2 fibroblasts induced differently sized tumors (Figures 5E and 5F). The presence of caNrf2 fibroblasts in these tumors was confirmed using immunofluorescence staining with an antibody against GFP, which is weakly expressed by caNrf2 expressing cells due to the inclusion of an IRES-GFP sequence downstream of the caNrf2 cDNA (Figures 1A and 5G) (Schäfer et al., 2012). Due to the low expression of GFP, the number of GFP-positive cells is likely to be underestimated.

Nrf2 Activation in Fibroblasts Alters ECM Protein Expression and Secretion

In search for the Nrf2 target genes that might be responsible for induction of senescence and the CAF phenotype, we further

Figure 4. caNrf2 in Fibroblasts Promotes Keratinocyte Proliferation and Accelerates Wound Closure

(A) Histological examination of wounds from ctrl and caNrf2 mice at either 5 or 14 days post-wounding stained using H&E, α smooth muscle actin (αSMA) immunofluorescence, SA-β-gal histochemistry, Ki67 immunofluorescence/immunohistochemistry, Meca32 immunofluorescence, or alkaline phosphatase histochemistry (ARE hPAP). PDGFRα-eGFP expressing mice were used for analysis of fibroblast proliferation. Black/white arrowheads indicate the front edge of the migrating epithelium. Dotted lines indicate the dermal-epidermal junction.

(B) Histological quantification of open versus closed wounds at day 5 post-injury (N = 15 mice, n = 23–27 wounds) and morphometric analysis of wounds at day 5 (N = 8–9; n = 8–9).

(C) Morphometric analysis of wounds at day 14 (N = 5–6; n = 5–6).

(D–F) Quantification of SA-β-gal-positive cells in the granulation tissue (N = 4; n = 4) (D), Ki67-positive fibroblasts in the granulation tissue (N = 7–8; n = 7–8) (E), and Ki67-positive keratinocytes (N = 4–6; n = 4–6) (F) in the migrating epidermis of 5-day wounds.

(G) BrdU-positive primary murine keratinocytes upon incubation with conditioned medium from caNrf2 or ctrl fibroblasts (N = 6–9 conditioned media samples from fibroblasts isolated from different mice). Nuclei were counterstained with propidium iodide.

(H) Area covered by Meca32-positive endothelial cells in the granulation tissue (in percentage of total area) (N = 5–6 mice, n = 5–6 wounds).

(I) Flow-cytometric analysis of the immune cell composition in 5-day wounds (N = 3; n = 3).

$^{**}p < 0.01$, $^{*}p < 0.05$, Mann-Whitney U test (all graphs, except analysis of open versus closed wounds for which Fisher's exact test was used). Bar graphs show mean and SEM. Scale bars, 200 μm (A) and 50 μm (G). See also Figures S2 and S3.

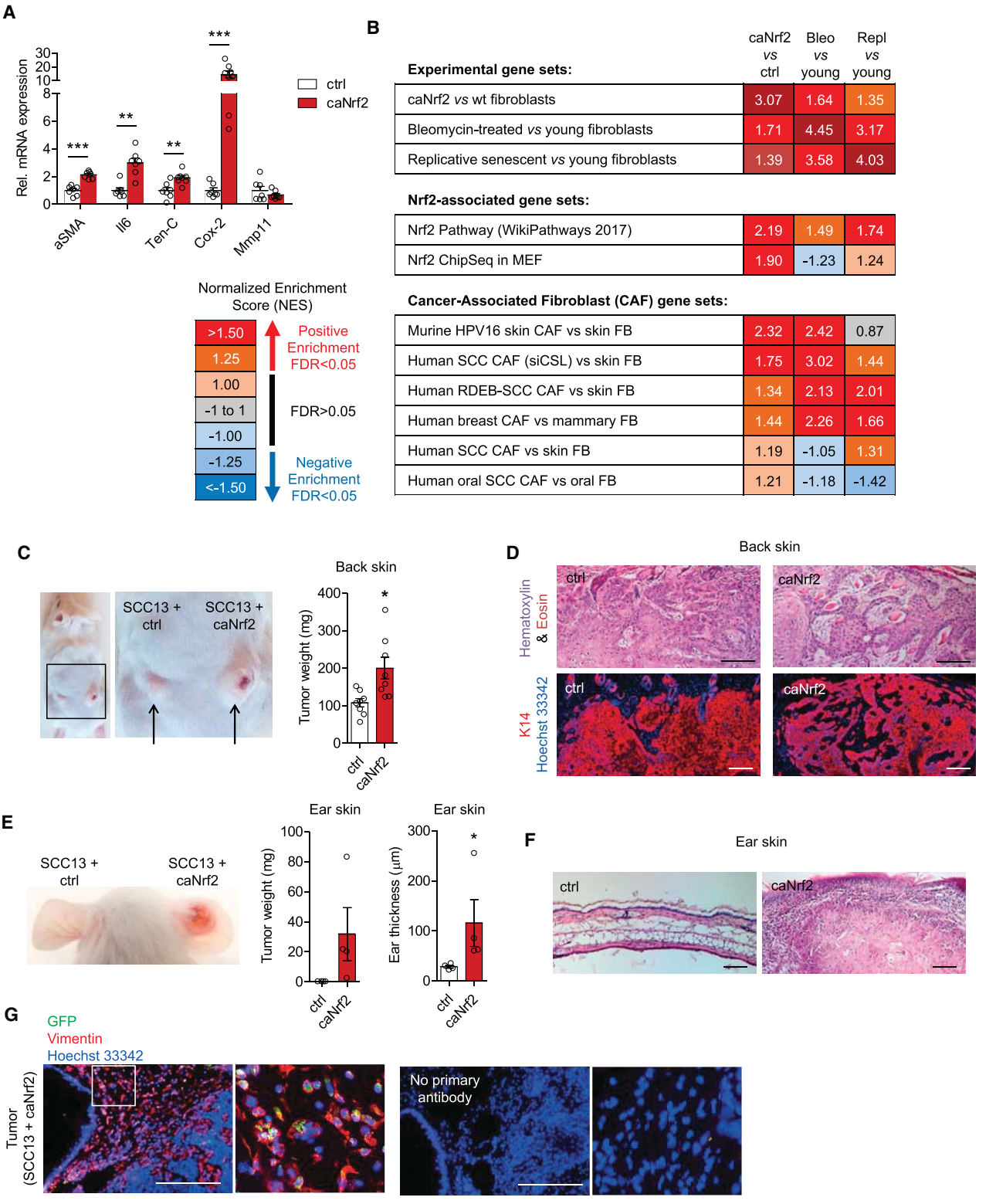

Figure 5. Nrf2-Mediated Fibroblast Senescence Leads to a CAF Phenotype

(A) Gene expression of several common CAF markers in caNrf2 versus ctrl fibroblasts analyzed by qRT-PCR (N = 7–8 cultures from different mice).

(B) Comparison of genes differentially expressed in caNrf2 fibroblasts with published datasets from bleomycin-induced senescent fibroblasts (Bleo) and from fibroblasts that have undergone replicative senescence (Repl), data published in an Nrf2 ChIP-seq study, genes involved in the Nrf2 pathway, or genes upregulated in various published CAF datasets from both mice and humans.

(legend continued on next page)

analyzed our RNA-seq data. Gene ontology enrichment analysis revealed a strong enrichment for extracellular components, including the ECM (Table S3). An overall decrease in most collagens was observed, including the main skin collagens type I and type III (Figures S4C–S4E). Expression of several major proteoglycans (e.g., asporin, biglycan, and versican) was also decreased, while various glycoproteins and other ECM-associated/secreted factors were either up- or downregulated (Figures S4C and S4D).

The strong effect of Nrf2 on the ECM was verified at the protein level using mass spectrometry-based proteomics of the ECM deposited by caNrf2 and ctrl fibroblasts, where major differences were observed (Figure 6A). Changes in gene expression do not always reflect similar changes in protein, and this was also observed when we compared the RNA-seq and the proteomics data. Nevertheless, 68 genes were upregulated at the RNA and protein level, while overlap was observed for 25 downregulated genes (Figures 6B, 6C, S4E, and S4F). Upregulated ECM proteins included activated leukocyte cell adhesion molecule (Alcam/CD166), UDP glucuronosyltransferase 1 family, polypeptide A7C (Ugt1a7c), cadherin-2, glypican-1, and plasminogen activator inhibitor-1 (PAI-1), and downregulated ECM components included the collagen chaperone heat shock protein 47 (Hsp47/Serpinh1), collagens type I and III, fibronectin and elastin (Figures S4E and S4F). Comparison of the upregulated genes and ECM proteins with previously published ChIP-seq datasets revealed the strongest correlation with Nrf2 ChIP-seq data from mouse embryonic fibroblasts, suggesting some of the differentially regulated genes as direct Nrf2 targets (Figure S4G; Table S4). Indeed, pathway analysis showed the strongest correlation of these proteins with the Nrf2 pathway (Figure S4H; Table S4). The ECM proteins affected by Nrf2 also correlated with those published for other senescent fibroblasts (Figure 6D). Specifically, correlations were observed for collagens I, III, and V, periostin, and Htra serine peptidase 3 (downregulated), while PAI-1 was increased across all examined senescence datasets and in caNrf2 ECM as well (Figure 6D). Herovici's stain indeed demonstrated a reduced collagen content in 5- and 14-day wounds from caNrf2 mice (Figures 6E and 6F). This was confirmed by biochemical analysis of skin samples, which also showed a reduced content of non-collagenous proteins in caNrf2 mice (Figure 6G). Furthermore, a higher susceptibility to collagenase digestion was demonstrated, suggesting possible differences in collagen processing or assembly (Figure 6G). Indeed, the post-translational modification of collagen was altered in caNrf2 mice, while analysis of collagen crosslinking, including hydroxylysine-aldehyde-derived collagen crosslinks (HP, DHLNL) only showed mild differences (Figures 6G, S5A, and S5B). Overall, collagen production and processing are significantly altered in caNrf2 fibroblasts, demonstrating an important role for Nrf2 in controlling the major ECM component of the skin.

ECM from caNrf2 Fibroblasts Promotes Senescence of Wild-Type Cells via PAI-1

To see if the ECM produced by caNrf2 fibroblasts influences senescence, wild-type fibroblasts were directly plated onto dishes coated with ECM deposited by either ctrl or caNrf2 fibroblasts (Figure 7A). Fibroblasts grown on caNrf2 ECM were significantly reduced in number during the second passage and showed a lower proliferation rate (Figures S6A and S6B). Most importantly, wild-type fibroblasts grown on caNrf2 ECM displayed significantly more SA-β-gal-positive cells when compared with cells grown on ctrl ECM (Figure 7B).

Among the ECM proteins upregulated at the RNA and protein level, the serine protease inhibitor PAI-1, also known as serpine1, attracted our attention, since extracellular PAI-1 was both necessary and sufficient to induce senescence in fibroblasts (Kortlever et al., 2006). Therefore, we treated ECM deposited by caNrf2 and ctrl cells with the PAI-1 antagonist geodin (Shinohara et al., 2000). Geodin treatment had little effect when added to ctrl ECM; however, geodin treatment of caNrf2 ECM completely restored the number of senescent cells to that seen in untreated or vehicle-treated ctrl ECM as shown by SA-β-gal staining (Figure 7C). 5-Bromo-2′-deoxyuridine incorporation showed similar, albeit non-significant tendencies (Figure 7D). We found increased PAI-1 staining, especially in extracellular spaces of the granulation tissue of 5-day wounds in caNrf2 mice, suggesting PAI-1 as a possible mediator of senescence *in vivo* (Figure S6C). No clear difference in PAI-1 staining was observed in unwounded skin at sites where senescent fibroblasts are not readily observed (Figure S6D). Together, these results demonstrate the remarkable impact of ECM produced by caNrf2 fibroblasts on the induction of senescence and point to PAI-1 as a major player in this process.

Nrf2 Directly Targets Genes Involved in ECM Remodeling

To determine whether Nrf2 directly induces transcription of ECM genes, we first identified eight upregulated ECM genes that were also upregulated at the protein level and organized them into their corresponding matrisome categories (Figure 7E). A search of DNA for potential Nrf2 binding sites (AREs) showed several genes that contained AREs <1 kb upstream of their transcription start sites (TSS) (Figure 7F). ChIP using lysates from primary skin fibroblasts and two different antibodies against Nrf2 showed evidence of Nrf2 binding to the AREs upstream of the TSS of the *PAI-1* gene as well as of other genes encoding ECM-affiliated

(C) SCC13 cells were co-injected with fibroblasts from ctrl or caNrf2 mice into back skin of mice. Tumor weight at week 5 after injection is shown (N = 8).
(D) Tumors from back skin examined by staining with H&E. Tumor cells were visualized by staining for the epithelial cell marker keratin 14 (red).
(E) SCC13 cells were co-injected with ctrl or caNrf2 fibroblasts into the ear of mice. Five weeks after injection tumors had formed only in ears injected with caNrf2 fibroblasts. Tumor weight and ear thickness are shown (N = 4).
(F) Ear skin/tumor sections stained with H&E.
(G) Immunofluorescence staining of sections from ear skin tumors formed in the presence of caNrf2 fibroblasts using antibodies against vimentin (red) and GFP (green). Nuclei were counterstained with Hoechst 33342 (blue).
Bar graphs show mean and SEM. *p < 0.05, **p < 0.01, ***p < 0.001, Mann-Whitney U test (A) or paired Student's t test (C and E). Scale bars, 100 μm. See also Figure S4 and Table S2.

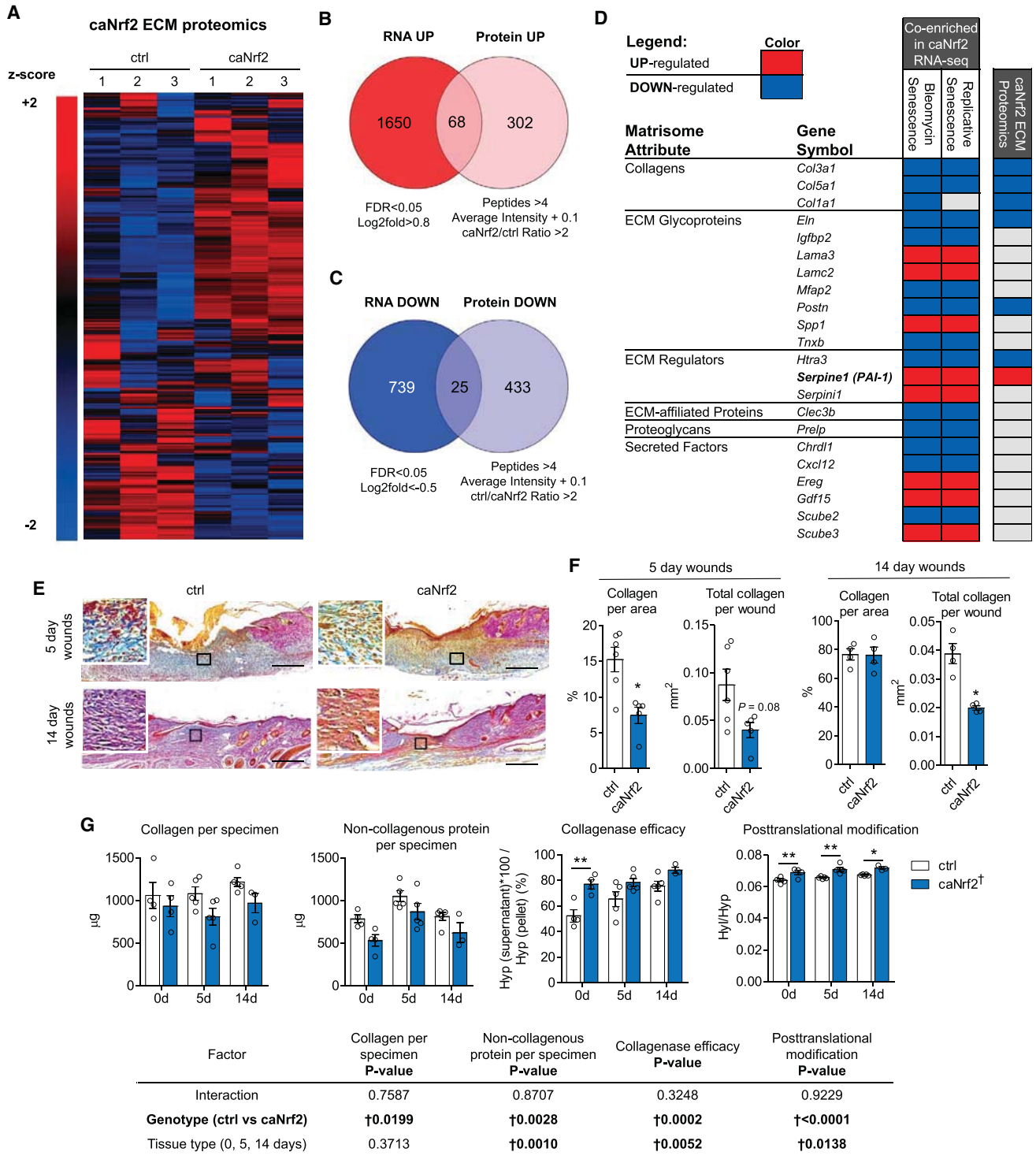

Factor	Collagen per specimen **P-value**	Non-collagenous protein per specimen **P-value**	Collagenase efficacy **P-value**	Posttranslational modification **P-value**
Interaction	0.7587	0.8707	0.3248	0.9229
Genotype (ctrl vs caNrf2)	**†0.0199**	**†0.0028**	**†0.0002**	**†<0.0001**
Tissue type (0, 5, 14 days)	0.3713	**†0.0010**	**†0.0052**	**†0.0138**

Figure 6. Nrf2 Controls ECM Protein Expression and Secretion in Fibroblasts

(A) Heatmap of log2 transformed, *Z* score normalized LFQ abundances of ECM proteins identified in the proteomics screen in ctrl versus caNrf2 fibroblast-deposited ECM (N = 3 cultures from different mice).

(B and C) Comparison of up- (B) and downregulated (C) genes (RNA-seq) with the corresponding ECM proteins (proteomics) identified 68 common upregulated ECM components and 25 downregulated ECM components.

(D) Differentially expressed matrisome genes in caNrf2 fibroblasts compared with published datasets from bleomycin-induced senescent fibroblasts, fibroblasts that have undergone replicative senescence and ECM proteins deposited by caNrf2 fibroblasts.

(legend continued on next page)

proteins (*Angptl2* [angiopoietin-like 2] and *Gpc1* [glypican 1]) (Figures 7G and 7H). qRT-PCR confirmed increased *PAI-1* mRNA levels in caNrf2 fibroblasts as well as in wild-type fibroblasts treated with the Nrf2 activator tBHQ (Figure S6E). Ko fibroblasts showed a slight, although non-significant reduction of *PAI-1* gene expression (Figure S6E). Taken together, these results demonstrate that Nrf2 activation in fibroblasts increases the production of a substantial number of ECM components/regulators, some of which are direct Nrf2 targets. These findings suggest that Nrf2 triggers a major senescence pathway, which results in expression of a SASP with consequently accelerated wound healing, but also increased tumor expansion (Figure 7I).

DISCUSSION

We identified an unexpected role of Nrf2 in the control of fibroblast senescence and induction of a CAF phenotype through regulation of the matrisome. The remarkable effect of Nrf2 on the matrix is a previously unrecognized function of this transcription factor.

Previous studies have demonstrated the impact of selected ECM proteins on senescence (Choi et al., 2011; Jun and Lau, 2010). For example, the matricellular protein CCN1 promoted fibroblast senescence during wound healing via a ROS-dependent mechanism (Jun and Lau, 2010). However, we observed reduced ROS levels in senescent caNrf2 fibroblasts and failed to detect differences in CCN1 expression, suggesting that fundamentally different mechanisms of senescence induction are involved. Indeed, Nrf2 activation induced the deposition of an ECM that promoted senescence, with PAI-1 being a key component. These changes in the matrisome reprogram fibroblasts into senescent cells and CAFs, a change that manifests itself profoundly during wound repair and tumorigenesis.

A previous study showed that PAI-1 is both necessary and sufficient to induce fibroblast senescence through inhibition of signaling via the phosphoinositide 3-kinase–protein kinase B–glycogen synthase kinase-3β–cyclin D1 pathway (Kortlever et al., 2006). Senescence and premature aging in Klotho-deficient mice was also mediated through PAI-1 (Eren et al., 2014). Our data demonstrate that increased PAI-1 not only promotes senescence, but that PAI-1 antagonists can be used to inhibit senescence in fibroblasts. Most importantly, it provides the first link between activated Nrf2 and this important senescence-promoting protein. Consistent with our results, PAI-1 inhibition caused delayed wound closure upon skin injury (Simone et al., 2015). However, PAI-1 knockout mice showed accelerated wound healing, and PAI-1 inhibition accelerated wound closure in diabetic mice through promotion of re-epithelialization (Chan et al., 2001; Rebalka et al., 2015). The role of PAI-1 in fibroblast senescence has, however, not been investigated in these studies. This is important, since other cells, including keratinocytes, also produce PAI-1 during wound healing, and different cell types may be differently affected by loss of PAI-1 (Romer et al., 1991; Staiano-Coico et al., 1996). The identification of *PAI-1* as an Nrf2 target gene raises the intriguing possibility that the positive effect of Nrf2-activating compounds or Keap-1 knockdown on wound healing in diabetic mice (Long et al., 2016; Rabbani et al., 2017; Soares et al., 2016) could be mediated in part via PAI-1 upregulation in fibroblasts. While this may be positive for wound healing, it could also stimulate cancer growth as suggested by our study and by the finding that increased PAI-1 levels in breast cancer samples are associated with poor prognosis (Foekens et al., 2000; Look et al., 2003).

The importance of senescence during wound repair in the skin has been demonstrated by selective removal of all p16-expressing senescent cells in mice, including, but not limited to fibroblasts (Demaria et al., 2014). In that study, senescent cells expressing PDGF-AA affected myofibroblast differentiation and contraction, and their removal lead to slower wound closure rates. We demonstrate that an increased presence of senescent fibroblasts resulting from constitutive activation of Nrf2 causes the reverse phenotype, featuring faster wound closure rates and less scar tissue at later stages. Our findings also suggest that induction of senescence specifically in fibroblasts is sufficient to promote wound healing. While *Pdfga* gene expression is also slightly increased in caNrf2 fibroblasts, we did not observe significant differences in myofibroblast differentiation or contraction. Instead, wound closure was affected primarily by differences in re-epithelialization and keratinocyte proliferation. The different results may be explained by the specific targeting of mesenchymal stromal cells in our study or by the existence of different subtypes of senescent cells, which express different secreted factors. The reduction in collagen deposition in caNrf2 wounds further suggests that Nrf2 activation in fibroblasts not only promotes wound healing, but also limits scarring/fibrosis.

The effect of caNrf2 fibroblasts on the epithelium is consistent with the known effect of fibroblasts producing a SASP, which includes a plethora of keratinocyte mitogens, cytokines, and growth factors capable of directly promoting epithelial cell proliferation (Coppe et al., 2010). Inflammation, which plays a critical role during wound healing (Eming et al., 2007; Martin, 1997), may also be affected by the SASP. The limited differences observed in immune cell content at day 5, however, combined with our tumor data in immunocompromised mice suggest that, in this case, the SASP is acting primarily by direct communication with keratinocytes.

Traditional conceptions of fibroblast senescence involve changes not observed in caNrf2 fibroblasts, such as cellular hypertrophy and increased intracellular ROS. This is paradoxical at first, particularly since multiple studies have demonstrated the effects of increased ROS on the onset of senescence, including through inhibition of the Nrf2 pathway. Under certain culture conditions, particularly when exposed to oxidative stress, Nrf2 inhibition indeed caused an early onset of senescence, and in some

(E and F) Five- and 14-day wound sections from ctrl and caNrf2 mice stained using the Herovici stain for collagen and quantification of positively stained pixels (blue/purple) expressed either as the percentage of total pixels (all colors) or as the absolute area in mm^2 of positively stained (blue/purple) tissue (N = 5–6 mice; n = 5–6 wounds). *$p < 0.05$, Mann-Whitney U test.

(G) Biochemical analysis of collagen content and modification in unwounded skin versus 5- and 14-day wounds (N = 4–5; n = 4–5, caNrf2 14d N = 3; n = 3). **$p < 0.01$, *$p < 0.05$, $^{\dagger}p < 0.05$, two-way ANOVA with Bonferroni post-test.

Bar graphs show mean and SEM. Scale bars, 200 μm. See also Figures S4 and S5 and Tables S2, S3, and S4.

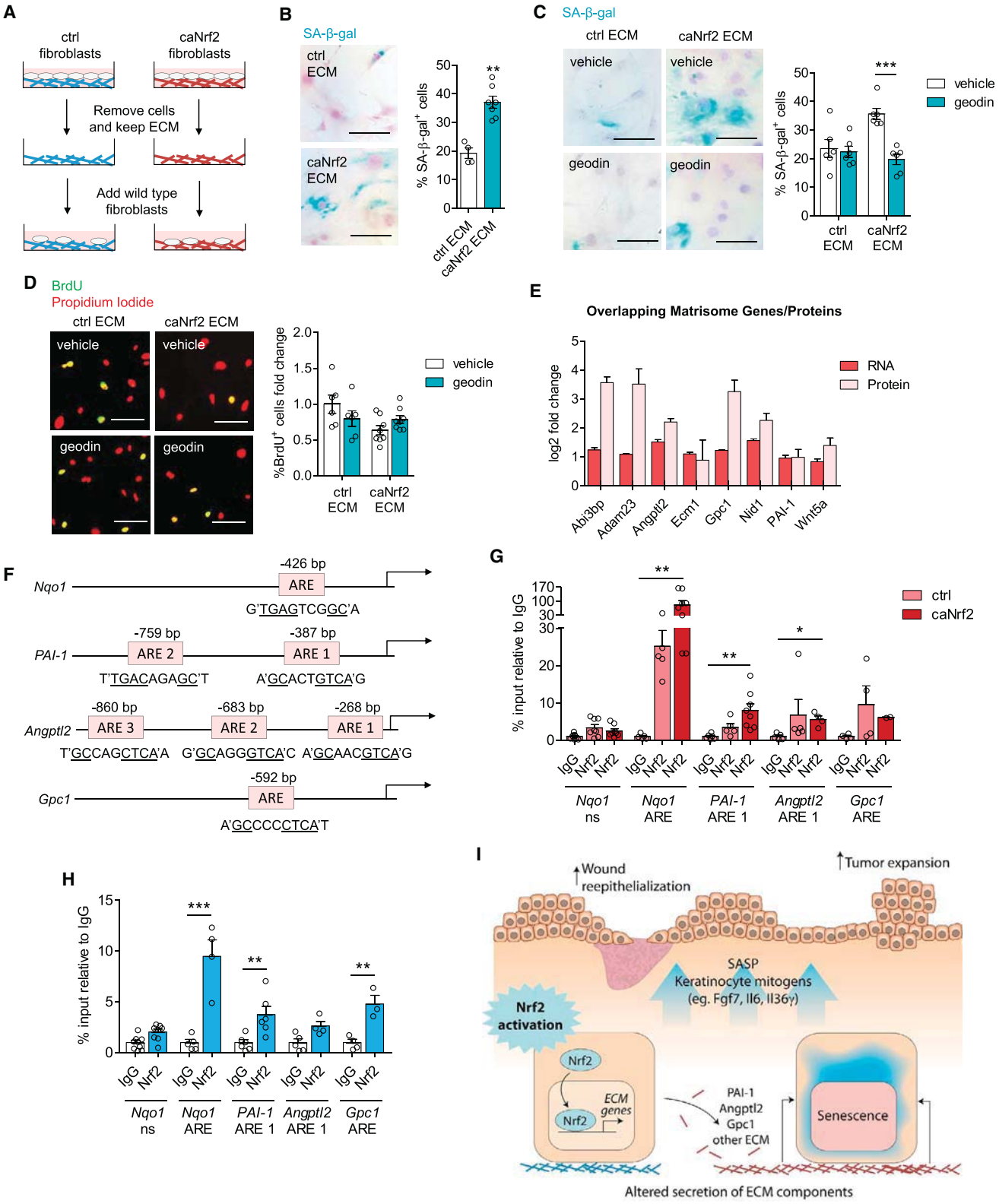

Figure 7. Nrf2 Targets Extracellular Matrix Genes to Promote Fibroblast Senescence

(A–D) Skin fibroblasts were isolated from wild-type mice and directly plated onto dishes coated with ECM deposited by either ctrl or caNrf2 fibroblasts. (A) Schematic representation of the experimental setup. (B) SA-β-gal staining of fibroblasts after two passages on either ctrl or caNrf2 ECM (N = 4–7). (C and D)

(legend continued on next page)

cases Nrf2 activation delayed the onset of senescence (Jodar et al., 2011; Kapeta et al., 2010; Volonte et al., 2013; Wang et al., 2017; Yang et al., 2013). These apparent differences from our data likely reflect the specific context, including cell type, stresses to which these cells are exposed and the exact level of Nrf2 activation/inhibition achieved. They also suggest that senescence can be induced via different pathways and independent of ROS. Consistent with this assumption, reduced levels of mitochondrial ROS have been observed when senescence was induced in WI-38 fibroblasts by silencing of lamin B1 (Shimi et al., 2011).

Nrf2 activating compounds are being tested for their efficacy in cancer and neurodegenerative and inflammatory diseases, in particular through their protective effect on epithelial and neuronal cells and their anti-inflammatory activities (Gao et al., 2014). Surprisingly, however, the effect of Nrf2 activation of fibroblasts has not been investigated *in vivo*, and, therefore, our results fill an important gap in our knowledge on Nrf2. Despite the obvious benefits of Nrf2 activation, chronic activation of the Nrf2 pathway can be detrimental, since, for example, cancer cells gain protection against oxidative damage, even during the early stages of tumor formation (Rolfs et al., 2015). We also suggest that sustained, pharmacological activation of Nrf2 may lead to the false perception of chronic stress, leading to the induction of fibroblast senescence and CAF activation. Indeed, our bioinformatics analysis identified Nrf2 activation as a previously unrecognized hallmark of the CAF phenotype in murine and also in different types of human cancers.

In summary, we highlight the profound effect of skin fibroblasts on the surrounding epithelium and demonstrate that activation of the here discovered Nrf2-ECM-senescence axis should be considered as a potential positive or negative consequence when NRF2 activating compounds are employed in the clinic.

STAR★METHODS

Detailed methods are provided in the online version of this paper and include the following:

SUPPLEMENTAL INFORMATION

Supplemental Information includes seven figures and four tables and can be found with this article online at https://doi.org/10.1016/j.devcel.2018.06.012.

ACKNOWLEDGMENTS

We thank Dr. Svitlana Kurinna, ETH Zurich, for help with the ChIP experiments, Prof. Gian-Paolo Dotto and Pino Bordignon, University of Lausanne, for help with ear tumorigenesis experiments, Joohee Lee and Christiane Born-Berclaz, ETH Zurich, for invaluable experimental help, and Drs. Hubert Rehrauer, Jelena Kühn Georgijevic, and Francesc Castro-Giner (Functional Genomics Center Zurich) for RNA sequencing. We further thank Dr. Shyam Biswal, Johns Hopkins University, Baltimore, MD, for the conditional *Nrf2* knockout mice and Drs. Jeffrey and Delinda Johnson, University of Wisconsin-Madison, WI, for ARE reporter mice. This work was supported by grants from the Swiss National Science Foundation (310030_132884 and 31003A_169204 to S.W.), the Wilhelm Sander-Stiftung (to S.W.), the Swiss Cancer League (KFS-3474-08-2014 to S.W.), and a Banting postdoctoral fellowship (to P.H.).

Wild-type fibroblasts stained for SA-β-gal (C) or analyzed for BrdU incorporation (D) after culture on ctrl versus caNrf2 ECM pre-treated with either vehicle or geodin for two passages (N = 6 for SA-β-gal and N = 6–8 for BrdU).

(E) Matrisome genes/proteins upregulated on the RNA and protein level in caNrf2 fibroblasts and in ECM deposited by caNrf2 fibroblasts (N = 3 cultures per genotype from different mice).

(F) Scheme showing the position of the AREs examined using ChIP.

(G) ChIP on ctrl fibroblasts using an antibody recognizing endogenous Nrf2 (N = 4–8 ChIPs).

(H) ChIP on ctrl and caNrf2 fibroblasts using an anti-Nrf2 antibody recognizing both endogenous Nrf2 and caNrf2 (N = 5–8).

(I) Proposed mechanism of Nrf2-mediated fibroblast senescence during wound healing and tumorigenesis. Nrf2 activation induces the expression of different matrix and matrix-remodeling genes resulting in an altered ECM. The altered matrix promotes fibroblast senescence with PAI-1 playing a particularly important role. Senescent fibroblasts produce a SASP, which promotes keratinocyte proliferation during wound healing and skin tumorigenesis, thereby promoting wound re-epithelialization and tumor expansion.

*$p < 0.05$, **$p < 0.01$, ***$p < 0.001$, Mann-Whitney U test (B, F, G, and H) or two-way ANOVA with Bonferroni post-test (C). Bar graphs show mean and SEM. Scale bars, 50 μm. See also Figure S6.

AUTHOR CONTRIBUTIONS

P.H., M.C., E.H., E.M., M.S., and J.B. performed the experiments. P.H., M.W., J.B., D.K., and J.D. analyzed the data. S.G. and H.-D.B. provided human primary fibroblasts and the lentiviral caNrf2 and CRISPR/Cas9 KEAP1-ko constructs, P.A. provided Col1α2Cre mice. D.K. conceived and supervised the back skin tumor experiments. J.D. conceived and supervised the proteomics experiments. P.H. and S.W. conceived the overall study and experimental design and wrote the manuscript. All co-authors made important comments to the manuscript.

DECLARATION OF INTERESTS

The authors have declared that no conflict of interest exists.

Received: January 8, 2018
Revised: May 14, 2018
Accepted: June 14, 2018
Published: July 16, 2018

REFERENCES

Bavik, C., Coleman, I., Dean, J.P., Knudsen, B., Plymate, S., and Nelson, P.S. (2006). The gene expression program of prostate fibroblast senescence modulates neoplastic epithelial cell proliferation through paracrine mechanisms. Cancer Res. *66*, 794–802.

Brinckmann, J., Kim, S., Wu, J., Reinhardt, D.P., Batmunkh, C., Metzen, E., Notbohm, H., Bank, R.A., Krieg, T., and Hunzelmann, N. (2005). Interleukin 4 and prolonged hypoxia induce a higher gene expression of lysyl hydroxylase 2 and an altered cross-link pattern: important pathogenetic steps in early and late stage of systemic scleroderma? Matrix Biol. *24*, 459–468.

Chan, J.C., Duszczyszyn, D.A., Castellino, F.J., and Ploplis, V.A. (2001). Accelerated skin wound healing in plasminogen activator inhibitor-1-deficient mice. Am. J. Pathol. *159*, 1681–1688.

Chen, L., Mirza, R., Kwon, Y., DiPietro, L.A., and Koh, T.J. (2015). The murine excisional wound model: contraction revisited. Wound Repair Regen. *23*, 874–877.

Choi, H.R., Cho, K.A., Kang, H.T., Lee, J.B., Kaeberlein, M., Suh, Y., Chung, I.K., and Park, S.C. (2011). Restoration of senescent human diploid fibroblasts by modulation of the extracellular matrix. Aging Cell *10*, 148–157.

Coppe, J.P., Desprez, P.Y., Krtolica, A., and Campisi, J. (2010). The senescence-associated secretory phenotype: the dark side of tumor suppression. Annu. Rev. Pathol. *5*, 99–118.

Cox, J., and Mann, M. (2008). MaxQuant enables high peptide identification rates, individualized p.p.b.-range mass accuracies and proteome-wide protein quantification. Nat. Biotechnol. *26*, 1367–1372.

Debacq-Chainiaux, F., Erusalimsky, J.D., Campisi, J., and Toussaint, O. (2009). Protocols to detect senescence-associated beta-galactosidase (SA-betagal) activity, a biomarker of senescent cells in culture and in vivo. Nat. Protoc. *4*, 1798–1806.

Demaria, M., Ohtani, N., Youssef, S.A., Rodier, F., Toussaint, W., Mitchell, J.R., Laberge, R.M., Vijg, J., Van Steeg, H., Dolle, M.E., et al. (2014). An essential role for senescent cells in optimal wound healing through secretion of PDGF-AA. Dev. Cell *31*, 722–733.

Dobin, A., Davis, C.A., Schlesinger, F., Drenkow, J., Zaleski, C., Jha, S., Batut, P., Chaisson, M., and Gingeras, T.R. (2013). STAR: ultrafast universal RNA-seq aligner. Bioinformatics *29*, 15–21.

Edgar, R., Domrachev, M., and Lash, A.E. (2002). Gene Expression Omnibus: NCBI gene expression and hybridization array data repository. Nucleic Acids Res. *30*, 207–210.

Eming, S.A., Krieg, T., and Davidson, J.M. (2007). Inflammation in wound repair: molecular and cellular mechanisms. J. Invest. Dermatol. *127*, 514–525.

Eren, M., Boe, A.E., Murphy, S.B., Place, A.T., Nagpal, V., Morales-Nebreda, L., Urich, D., Quaggin, S.E., Budinger, G.R., Mutlu, G.M., et al. (2014). PAI-1-regulated extracellular proteolysis governs senescence and survival in Klotho mice. Proc. Natl. Acad. Sci. USA *111*, 7090–7095.

Florin, L., Alter, H., Grone, H.J., Szabowski, A., Schutz, G., and Angel, P. (2004). Cre recombinase-mediated gene targeting of mesenchymal cells. Genesis *38*, 139–144.

Foekens, J.A., Peters, H.A., Look, M.P., Portengen, H., Schmitt, M., Kramer, M.D., Brunner, N., Janicke, F., Meijer-van Gelder, M.E., Henzen-Logmans, S.C., et al. (2000). The urokinase system of plasminogen activation and prognosis in 2780 breast cancer patients. Cancer Res. *60*, 636–643.

Gao, B., Doan, A., and Hybertson, B.M. (2014). The clinical potential of influencing Nrf2 signaling in degenerative and immunological disorders. Clin. Pharmacol. *6*, 19–34.

Garstkiewicz, M., Strittmatter, G.E., Grossi, S., Sand, J., Fenini, G., Werner, S., French, L.E., and Beer, H.D. (2017). Opposing effects of Nrf2 and Nrf2-activating compounds on the NLRP3 inflammasome independent of Nrf2-mediated gene expression. Eur. J. Immunol. *47*, 806–817.

Hamilton, T.G., Klinghoffer, R.A., Corrin, P.D., and Soriano, P. (2003). Evolutionary divergence of platelet-derived growth factor alpha receptor signaling mechanisms. Mol. Cell. Biol. *23*, 4013–4025.

Herovici, C. (1963). Picropolychrome: histological staining technic intended for the study of normal and pathological connective tissue. Rev. Fr. Etud. Clin. Biol. *8*, 88–89.

Jodar, L., Mercken, E.M., Ariza, J., Younts, C., Gonzalez-Reyes, J.A., Alcain, F.J., Buron, I., de Cabo, R., and Villalba, J.M. (2011). Genetic deletion of Nrf2 promotes immortalization and decreases life span of murine embryonic fibroblasts. J. Gerontol. A Biol. Sci. Med. Sci. *66*, 247–256.

Johnson, D.A., Andrews, G.K., Xu, W., and Johnson, J.A. (2002). Activation of the antioxidant response element in primary cortical neuronal cultures derived from transgenic reporter mice. J. Neurochem. *81*, 1233–1241.

Jun, J.I., and Lau, L.F. (2010). The matricellular protein CCN1 induces fibroblast senescence and restricts fibrosis in cutaneous wound healing. Nat. Cell Biol. *12*, 676–685.

Kansanen, E., Kuosmanen, S.M., Leinonen, H., and Levonen, A.L. (2013). The Keap1-Nrf2 pathway: mechanisms of activation and dysregulation in cancer. Redox Biol. *1*, 45–49.

Kapeta, S., Chondrogianni, N., and Gonos, E.S. (2010). Nuclear erythroid factor 2-mediated proteasome activation delays senescence in human fibroblasts. J. Biol. Chem. *285*, 8171–8184.

Kohler, U.A., Kurinna, S., Schwitter, D., Marti, A., Schäfer, M., Hellerbrand, C., Speicher, T., and Werner, S. (2014). Activated Nrf2 impairs liver regeneration in mice by activation of genes involved in cell-cycle control and apoptosis. Hepatology *60*, 670–678.

Kortlever, R.M., Higgins, P.J., and Bernards, R. (2006). Plasminogen activator inhibitor-1 is a critical downstream target of p53 in the induction of replicative senescence. Nat. Cell Biol. *8*, 877–884.

Krtolica, A., Parrinello, S., Lockett, S., Desprez, P.Y., and Campisi, J. (2001). Senescent fibroblasts promote epithelial cell growth and tumorigenesis: a link between cancer and aging. Proc. Natl. Acad. Sci. USA *98*, 12072–12077.

Kuleshov, M.V., Jones, M.R., Rouillard, A.D., Fernandez, N.F., Duan, Q., Wang, Z., Koplev, S., Jenkins, S.L., Jagodnik, K.M., Lachmann, A., et al. (2016). Enrichr: a comprehensive gene set enrichment analysis web server 2016 update. Nucleic Acids Res. *44*, W90–W97.

Laberge, R.M., Awad, P., Campisi, J., and Desprez, P.Y. (2012). Epithelial-mesenchymal transition induced by senescent fibroblasts. Cancer Microenviron. *5*, 39–44.

Lee, D.F., Kuo, H.P., Liu, M., Chou, C.K., Xia, W., Du, Y., Shen, J., Chen, C.T., Huo, L., Hsu, M.C., et al. (2009). KEAP1 E3 ligase-mediated downregulation of NF-kappaB signaling by targeting IKKbeta. Mol. Cell *36*, 131–140.

Li, B., and Dewey, C.N. (2011). RSEM: accurate transcript quantification from RNA-Seq data with or without a reference genome. BMC Bioinformatics *12*, 323.

Liby, K.T., and Sporn, M.B. (2012). Synthetic oleanane triterpenoids: multifunctional drugs with a broad range of applications for prevention and treatment of chronic disease. Pharmacol. Rev. *64*, 972–1003.

Liu, D., and Hornsby, P.J. (2007). Senescent human fibroblasts increase the early growth of xenograft tumors via matrix metalloproteinase secretion. Cancer Res. *67*, 3117–3126.

Long, M., Rojo de la Vega, M., Wen, Q., Bharara, M., Jiang, T., Zhang, R., Zhou, S., Wong, P.K., Wondrak, G.T., Zheng, H., et al. (2016). An essential role of NRF2 in diabetic wound healing. Diabetes *65*, 780–793.

Look, M., van Putten, W., Duffy, M., Harbeck, N., Christensen, I.J., Thomssen, C., Kates, R., Spyratos, F., Ferno, M., Eppenberger-Castori, S., et al. (2003). Pooled analysis of prognostic impact of uPA and PAI-1 in breast cancer patients. Thromb. Haemost. *90*, 538–548.

Macip, S., Igarashi, M., Fang, L., Chen, A., Pan, Z.Q., Lee, S.W., and Aaronson, S.A. (2002). Inhibition of p21-mediated ROS accumulation can rescue p21-induced senescence. EMBO J. *21*, 2180–2188.

Malhotra, D., Portales-Casamar, E., Singh, A., Srivastava, S., Arenillas, D., Happel, C., Shyr, C., Wakabayashi, N., Kensler, T.W., Wasserman, W.W., et al. (2010). Global mapping of binding sites for Nrf2 identifies novel targets in cell survival response through ChIP-Seq profiling and network analysis. Nucleic Acids Res. *38*, 5718–5734.

Martin, P. (1997). Wound healing – aiming for perfect skin regeneration. Science *276*, 75–81.

Mulvaney, K.M., Matson, J.P., Siesser, P.F., Tamir, T.Y., Goldfarb, D., Jacobs, T.M., Cloer, E.W., Harrison, J.S., Vaziri, C., Cook, J.G., et al. (2016). Identification and characterization of MCM3 as a Kelch-like ECH-associated protein 1 (KEAP1) substrate. J. Biol. Chem. *291*, 23719–23733.

Orthwein, A., Noordermeer, S.M., Wilson, M.D., Landry, S., Enchev, R.I., Sherker, A., Munro, M., Pinder, J., Salsman, J., Dellaire, G., et al. (2015). A mechanism for the suppression of homologous recombination in G1 cells. Nature *528*, 422–426.

Papadopoulou, A., and Kletsas, D. (2011). Human lung fibroblasts prematurely senescent after exposure to ionizing radiation enhance the growth of malignant lung epithelial cells in vitro and in vivo. Int. J. Oncol. *39*, 989–999.

Parrinello, S., Coppe, J.P., Krtolica, A., and Campisi, J. (2005). Stromal-epithelial interactions in aging and cancer: senescent fibroblasts alter epithelial cell differentiation. J. Cell Sci. *118*, 485–496.

Pazolli, E., Luo, X., Brehm, S., Carbery, K., Chung, J.J., Prior, J.L., Doherty, J., Demehri, S., Salavaggione, L., Piwnica-Worms, D., et al. (2009). Senescent stromal-derived osteopontin promotes preneoplastic cell growth. Cancer Res. *69*, 1230–1239.

Procopio, M.G., Laszlo, C., Al Labban, D., Kim, D.E., Bordignon, P., Jo, S.H., Goruppi, S., Menietti, E., Ostano, P., Ala, U., et al. (2015). Combined CSL and p53 downregulation promotes cancer-associated fibroblast activation. Nat. Cell Biol. *17*, 1193–1204.

Qin, X.Y., Fukuda, T., Yang, L., Zaha, H., Akanuma, H., Zeng, Q., Yoshinaga, J., and Sone, H. (2012). Effects of bisphenol A exposure on the proliferation and senescence of normal human mammary epithelial cells. Cancer Biol. Ther. *13*, 296–306.

Rabbani, P.S., Zhou, A., Borab, Z.M., Frezzo, J.A., Srivastava, N., More, H.T., Rifkin, W.J., David, J.A., Berens, S.J., Chen, R., et al. (2017). Novel lipoproteoplex delivers Keap1 siRNA based gene therapy to accelerate diabetic wound healing. Biomaterials *132*, 1–15.

Rappsilber, J., Mann, M., and Ishihama, Y. (2007). Protocol for micro-purification, enrichment, pre-fractionation and storage of peptides for proteomics using StageTips. Nat. Protoc. *2*, 1896–1906.

Rebalka, I.A., Raleigh, M.J., D'Souza, D.M., Coleman, S.K., Rebalka, A.N., and Hawke, T.J. (2015). Inhibition of PAI-1 via PAI-039 improves dermal wound closure in diabetes. Diabetes *64*, 2593–2602.

Reddy, N.M., Potteti, H.R., Mariani, T.J., Biswal, S., and Reddy, S.P. (2011). Conditional deletion of Nrf2 in airway epithelium exacerbates acute lung injury and impairs the resolution of inflammation. Am. J. Respir. Cell Mol. Biol. *45*, 1161–1168.

Rheinwald, J.G., and Beckett, M.A. (1981). Tumorigenic keratinocyte lines requiring anchorage and fibroblast support cultured from human squamous cell carcinomas. Cancer Res. *41*, 1657–1663.

Robinson, M.D., McCarthy, D.J., and Smyth, G.K. (2010). edgeR: a Bioconductor package for differential expression analysis of digital gene expression data. Bioinformatics *26*, 139–140.

Rolfs, F., Huber, M., Kuehne, A., Kramer, S., Haertel, E., Muzumdar, S., Wagner, J., Tanner, Y., Bohm, F., Smola, S., et al. (2015). Nrf2 activation promotes keratinocyte survival during early skin carcinogenesis via metabolic alterations. Cancer Res. *75*, 4817–4829.

Romer, J., Lund, L.R., Eriksen, J., Ralfkiaer, E., Zeheb, R., Gelehrter, T.D., Dano, K., and Kristensen, P. (1991). Differential expression of urokinase-type plasminogen activator and its type-1 inhibitor during healing of mouse skin wounds. J. Invest. Dermatol. *97*, 803–811.

Schäfer, M., Dutsch, S., auf dem Keller, U., Navid, F., Schwarz, A., Johnson, D.A., Johnson, J.A., and Werner, S. (2010). Nrf2 establishes a glutathione-mediated gradient of UVB cytoprotection in the epidermis. Genes Dev. *24*, 1045–1058.

Schäfer, M., Farwanah, H., Willrodt, A.H., Huebner, A.J., Sandhoff, K., Roop, D., Hohl, D., Bloch, W., and Werner, S. (2012). Nrf2 links epidermal barrier function with antioxidant defense. EMBO Mol. Med. *4*, 364–379.

Schäfer, M., and Werner, S. (2008). Oxidative stress in normal and impaired wound repair. Pharmacol. Res. *58*, 165–171.

Schäfer, M., Willrodt, A.H., Kurinna, S., Link, A.S., Farwanah, H., Geusau, A., Gruber, F., Sorg, O., Huebner, A.J., Roop, D.R., et al. (2014). Activation of Nrf2 in keratinocytes causes chloracne (MADISH)-like skin disease in mice. EMBO Mol. Med. *6*, 442–457.

Shevchenko, A., Tomas, H., Havlis, J., Olsen, J.V., and Mann, M. (2006). In-gel digestion for mass spectrometric characterization of proteins and proteomes. Nat. Protoc. *1*, 2856–2860.

Shimi, T., Butin-Israeli, V., Adam, S.A., Hamanaka, R.B., Goldman, A.E., Lucas, C.A., Shumaker, D.K., Kosak, S.T., Chandel, N.S., and Goldman, R.D. (2011). The role of nuclear lamin B1 in cell proliferation and senescence. Genes Dev. *25*, 2579–2593.

Shinohara, C., Chikanishi, T., Nakashima, S., Hashimoto, A., Hamanaka, A., Endo, A., and Hasumi, K. (2000). Enhancement of fibrinolytic activity of vascular endothelial cells by chaetoglobosin A, crinipellin B, geodin and triticone B. J. Antibiot. (Tokyo) *53*, 262–268.

Simone, T.M., Longmate, W.M., Law, B.K., and Higgins, P.J. (2015). Targeted inhibition of PAI-1 activity impairs epithelial migration and wound closure following cutaneous injury. Adv. Wound Care (New Rochelle) *4*, 321–328.

Soares, M.A., Cohen, O.D., Low, Y.C., Sartor, R.A., Ellison, T., Anil, U., Anzai, L., Chang, J.B., Saadeh, P.B., Rabbani, P.S., et al. (2016). Restoration of Nrf2 signaling normalizes the regenerative niche. Diabetes *65*, 633–646.

Sporn, M.B., and Liby, K.T. (2012). NRF2 and cancer: the good, the bad and the importance of context. Nat. Rev. Cancer *12*, 564–571.

Staiano-Coico, L., Carano, K., Allan, V.M., Steiner, M.G., Pagan-Charry, I., Bailey, B.B., Babaar, P., Rigas, B., and Higgins, P.J. (1996). PAI-1 gene expression is growth state-regulated in cultured human epidermal keratinocytes during progression to confluence and postwounding. Exp. Cell Res. *227*, 123–134.

Suzuki, T., and Yamamoto, M. (2017). Stress-sensing mechanisms and the physiological roles of the Keap1-Nrf2 system during cellular stress. J. Biol. Chem. *292*, 16817–16824.

Sykiotis, G.P., and Bohmann, D. (2010). Stress-activated cap'n'collar transcription factors in aging and human disease. Sci. Signal. *3*, re3.

Taguchi, K., Motohashi, H., and Yamamoto, M. (2011). Molecular mechanisms of the Keap1-Nrf2 pathway in stress response and cancer evolution. Genes Cells *16*, 123–140.

Talalay, P., Fahey, J.W., Healy, Z.R., Wehage, S.L., Benedict, A.L., Min, C., and Dinkova-Kostova, A.T. (2007). Sulforaphane mobilizes cellular defenses that protect skin against damage by UV radiation. Proc. Natl. Acad. Sci. USA *104*, 17500–17505.

Telorack, M., Meyer, M., Ingold, I., Conrad, M., Bloch, W., and Werner, S. (2016). A glutathione-Nrf2-thioredoxin cross-talk ensures keratinocyte survival and efficient wound repair. PLoS Genet. *12*, e1005800.

Uhlen, M., Fagerberg, L., Hallstrom, B.M., Lindskog, C., Oksvold, P., Mardinoglu, A., Sivertsson, A., Kampf, C., Sjostedt, E., Asplund, A., et al. (2015). Proteomics. Tissue-based map of the human proteome. Science *347*, 1260419.

Uhlen, M., Zhang, C., Lee, S., Sjostedt, E., Fagerberg, L., Bidkhori, G., Benfeitas, R., Arif, M., Liu, Z., Edfors, F., et al. (2017). A pathology atlas of the human cancer transcriptome. Science *357*, https://doi.org/10.1126/science.aan2507.

Vizcaino, J.A., Csordas, A., del-Toro, N., Dianes, J.A., Griss, J., Lavidas, I., Mayer, G., Perez-Riverol, Y., Reisinger, F., Ternent, T., et al. (2016). 2016 update of the PRIDE database and its related tools. Nucleic Acids Res. *44*, D447–D456.

Volonte, D., Liu, Z., Musille, P.M., Stoppani, E., Wakabayashi, N., Di, Y.P., Lisanti, M.P., Kensler, T.W., and Galbiati, F. (2013). Inhibition of nuclear factor-erythroid 2-related factor (Nrf2) by caveolin-1 promotes stress-induced premature senescence. Mol. Biol. Cell *24*, 1852–1862.

Wang, R., Yu, Z., Sunchu, B., Shoaf, J., Dang, I., Zhao, S., Caples, K., Bradley, L., Beaver, L.M., Ho, E., et al. (2017). Rapamycin inhibits the secretory phenotype of senescent cells by a Nrf2-independent mechanism. Aging Cell *16*, 564–574.

Weyemi, U., Lagente-Chevallier, O., Boufraqech, M., Prenois, F., Courtin, F., Caillou, B., Talbot, M., Dardalhon, M., Al Ghuzlan, A., Bidart, J.M., et al. (2012). ROS-generating NADPH oxidase NOX4 is a critical mediator in oncogenic H-Ras-induced DNA damage and subsequent senescence. Oncogene *31*, 1117–1129.

Wondrak, G.T. (2009). Redox-directed cancer therapeutics: molecular mechanisms and opportunities. Antioxid. Redox Signal. *11*, 3013–3069.

Yang, G., Zhao, K., Ju, Y., Mani, S., Cao, Q., Puukila, S., Khaper, N., Wu, L., and Wang, R. (2013). Hydrogen sulfide protects against cellular senescence via S-sulfhydration of Keap1 and activation of Nrf2. Antioxid. Redox Signal. *18*, 1906–1919.

STAR★METHODS

KEY RESOURCES TABLE

REAGENT or RESOURCE	SOURCE	IDENTIFIER
Antibodies		
Rabbit anti-Ki67	Abcam	Cat#Ab15580; RRID:AB_443209
Rabbit anti-serpine1 (PAI-1)	Novus Biologicals	Cat#NBP1-19773; RRID:AB_1642775
Mouse anti-keratin 10	DAKO	Cat#M7002
Rabbit anti-keratin 14	BAbCo	Cat#PRB-155P; RRID:AB_292096
Rabbit anti-loricrin	Covance	Cat#PRB-145P; RRID:AB_10064155
Mouse anti-α-smooth muscle actin-FITC	Sigma	Cat#F3777; RRID:AB_476977
Rat anti-Meca32	BD Biosciences	Cat#553849; RRID:AB_395086
Rabbit anti-Nrf2	MyBioSource	Cat#MBS176387
Mouse anti-Brdu-FITC	Sigma	Cat#11202693001; RRID:AB_514484
Mouse anti-γH2A.X	Millipore	Cat#16-193; RRID:AB_310795
Biotinylated anti-rabbit IgG	Jackson	Cat#111-065-003; RRID:AB_2337959
Anti-rabbit Cy3	Jackson	Cat#711-165-152; RRID:AB_2307443
Anti-mouse Cy3	Jackson	Cat#715-165-150; RRID:AB_2340813
Anti-rabbit Cy2	Jackson	Cat#111-225-003; RRID:AB_2307385
Anti-CD45 AF700	BioLegend	Cat#103128; RRID:AB_493715
Anti-CD3 BV 785	BioLegend	Cat#100231; RRID:AB_11218805
Anti-TCRb APC-Cy7	BioLegend	Cat#109219; RRID:AB_893626
Anti-CD4 BV711	BioLegend	Cat#100447; RRID:AB_2564586
Anti-Ly6G FITC	BD Biosciences	Cat#551460; RRID:AB_394207
Anti-CD64 BV 421	BioLegend	Cat#139309; RRID:AB_2562694
Anti-NKp46 PCP-Cy5.5	BioLegend	Cat#137610; RRID:AB_10641137
Anti-CD19 BV 650	BioLegend	Cat#115541; RRID:AB_11204087
Anti-F4/80 AF 647	AbD Serotec	Cat#MCA497A647T; RRID:AB_1102555
Anti-CD11c PE-Cy7	BioLegend	Cat#117318; RRID:AB_493568
Anti-MHC II PE	BD BioSciences	Cat#557000; RRID:AB_396546
Anti-CD45 Pacific blue	BioLegend	Cat#103126; RRID:AB_493535
Anti-CD31 PE	eBiosciences	Cat#12-0311-82; RRID:AB_465632
Anti-CD140a APC	BioLegend	Cat#135908; RRID:AB_2043970
Anti-CD49f Biotin	BioLegend	Cat#313604; RRID:AB_345298
Streptavidin BV711	BD Biosciences	Cat#563262
Anti-CD140a BV605	BioLegend	Cat#135916; RRID:AB_2721548
Rabbit anti-Nrf2	SantaCruz	Cat#sc-722X; RRID:AB_2108502
Rabbit anti-Histone H3	Abcam	Cat#ab1791; RRID:AB_302613
Normal rabbit IgG	Millipore	Cat#12-370; RRID:AB_145841
Bacterial and Virus Strains		
One Shot TOP10	Invitrogen	Cat#C404003
Biological Samples		
All biological samples were generated in this study and described in detail in the Results	ETH Zürich	N/A
Chemicals, Peptides, and Recombinant Proteins		
Zombie Aqua live/dead stain for flow cytometry	BioLegend	Cat#423102
Sytox green live/dead stain for flow cytometry	Life Technologies	Cat#S34860
Fc block for flow cytometry	BD BioSciences	Cat#553142
Hoechst 33342	Sigma	Cat#B2261
Nuclear Fast Red	Sigma	Cat#N3020

(*Continued on next page*)

Continued

REAGENT or RESOURCE	SOURCE	IDENTIFIER
Propidium iodide	Sigma	Cat#P4170
H2DCFDA	Invitrogen	Cat#D399
tert-Butyl-hydroquinone (tBHQ)	Sigma	Cat#20021
Sulforaphane	Enzo Life Sciences	Cat#ALX-350-230-M010
CDDO-Im	Tocris Bioscience	Cat#4737
TRIzol Reagent	Invitrogen	Cat#15596018
Collagenase type 2 (CLS2)	Worthington Biochemical Corporation	Cat#LS004176
Liberase TL	Roche	Cat#05401020001
Trypsin-EDTA solution	Sigma	Cat#T4174
Geodin	Abcam	Cat#ab144263
BCIP/NBT colour development substrate	Promega	Cat#S3771
Critical Commercial Assays		
TruSeq RNA Sample Prep Kit v2	Illumina	Cat#RS-122-2001
TruSeq PE Cluster Kit HS4000	Illumina	Cat#PE-401-3001
TruSeq SR Cluster Kit HS4000	Illumina	Cat#GD-401-3001
TruSeq SBS Kit HS4000	Illumina	Cat#FC-401-3001
CellROX Orange ROS detection kit	Invitrogen	Cat#C10443
iScript cDNA synthesis kit	Biorad	Cat#1708890
Protease inhibitor mix cOmplete Mini	Roche	Cat#11836170001
Vectastain ABC kit	Vector Laboratories	Cat#PK-6100
DAB peroxidase substrate kit	Vector Laboratories	Cat#SK-4100
SYBR Green I Master Reaction Mix	Roche	Cat#04 707 516 001
KAPA2G FAST Genotyping Mix	Kapa Biosystems	Cat#KK5121
PCR Mycoplasma Test Kit I/C	PromoKine	Cat#PK-CA91-1096
Dynabeads Protein A	Thermo Fisher	Cat#10001D
Dynabeads Protein G	Thermo Fisher	Cat#10003D
Deposited Data		
Raw and analyzed mass spectrometry proteomics data	This paper	ProteomeXchange Consortium via the PRIDE (Vizcaino et al., 2016) partner repository with the dataset identifier PXD007999.
RNAseq data	This paper	NCBI's Gene Expression Omnibus (Edgar et al., 2002); accessible through GEO Series accession number GSE106097 (https://www.ncbi.nlm.nih.gov/geo/query/acc.cgi?acc=GSE106097).
Experimental Models: Cell Lines		
SCC13 Cutaneous squamous cell carcinoma cell line	Rheinwald and Beckett, 1981	N/A
Experimental Models: Organisms/Strains		
Mouse: Col1α2-Cre	Florin et al., 2004	N/A
Mouse: CMVcaNrf2	Schäfer et al., 2012	N/A
Mouse: ARE-hPAP	Johnson et al., 2002	N/A
Mouse: Nrf2-floxed	Reddy et al., 2011	N/A
Mouse: PDGFRα-eGFP	Hamilton et al., 2003	N/A
Oligonucleotides		
Genotyping PCR primers (Col1α2-Cre) 5′-TTA GCA CCA CGG CAG CAG GAG-3′ 5′-CAG GCC AGA TCT CCT GTG CAG CAT-3′	Microsynth AG	N/A
Genotyping PCR primers (caNrf2) 5′-CGG CTC AGC ACC TTG TAT C-3′ 5′-CTT ATT CCA AGC GGC TTC GGC-3′	Microsynth AG	N/A

(*Continued on next page*)

Continued

REAGENT or RESOURCE	SOURCE	IDENTIFIER
Genotyping PCR primers (ARE-hPAP) 5′-CTA GAG TCA CAG TGA CTT GGC AAA-3′ 5′-GGA AGATGATGAGGT CTC TGG CG-3′	Microsynth AG	N/A
Genotyping PCR primers (Nrf2-floxed) 5′-TCT TAG GCA CCA TTT GGG AGA-3′ 5′-TAC AGC AGG CAT ACC ATT GTG G-3′	Microsynth AG	N/A
Genotyping PCR primers (PDGFRα-eGFP) 5′-CCC TTG TGG TCA TGC CAA AC-3′ 5′-GCT TTT GCC TCC ATT ACA CTG G-3′ 5′-ACG AAG TTA TTA GGT CCC TCG AC-3′	Microsynth AG	N/A
Mouse qPCR primers (*Rps29*) 5′-GGT CAC CAG CAG CTC TAC TG-3′ 5′-GTC CAA CTT AAT GAA GCC TAT GTC C-3′	Microsynth AG	N/A
Mouse qPCR primers (*Nqo1*) 5′-GAC AAC GGT CCT TTC CAG AAT A-3′ 5′-CTC TGA ATC GGC CAG AGA ATG-3′	Microsynth AG	N/A
Mouse qPCR primers (*Gclc*) 5′-AAC AAG AAA CAT CCG GCA TC-3′ 5′-CGT AGC CTC GGT AAA ATG GA-3′	Microsynth AG	N/A
Mouse qPCR primers (*Gclm*) 5′-TCC CAT GCA GTG GAG AAG AT-3′ 5′-AGC TGT GCA ACT CCA AGG AC-3′	Microsynth AG	N/A
Mouse qPCR primers (*Srxn1*) 5′-CGG TGC ACA ACG TAC CAA T-3′ 5′-TTG ATC CAG AGG ACG TCG AT-3′	Microsynth AG	N/A
Mouse qPCR primers (*p15ink4b*) 5′-AGA TCC CAA CGC CCT GAA C-3′ 5′-CCC ATC ATC ATG ACC TGG ATT-3′	Microsynth AG	N/A
Mouse qPCR primers (*p16ink4a*) 5′-CGT ACC CCG ATT CAG GTG AT-3′ 5′-TTG AGC AGA AGA GCT GCT ACG T-3′	Microsynth AG	N/A
Mouse qPCR primers (*p21Cip1*) 5′-GTG ATT GCG ATG CGC TCA TG-3′ 5′-TCT CTT GCA GAA GAC CAA TC-3′	Microsynth AG	N/A
Mouse qPCR primers (*αSMA*) 5′-CTG CCG AGC GTG AGA TTG-3′ 5′-ATA GGT GGT TTC GTG GAT GC-3′	Microsynth AG	N/A
Mouse qPCR primers (*Col1a1*) 5′-TGT TCA GCT TTG ACC TCC GGC T-3′ 5′-TCT CCC TTG GGT CCC TCG ACT-3′	Microsynth AG	N/A
Mouse qPCR primers (*Col1a2*) 5′-CAC CCC AGC GAA GAA CTC ATA-3′ 5′-GCC ACC ATT GAT AGT CTC TCC-3′	Microsynth AG	N/A
Mouse qPCR primers (*Il6*) 5′-CCG GAG AGG AGA CTT CAC AG-3′ 5′-TTC TGC AAG TGC ATC ATC GT-3′	Microsynth AG	N/A
Mouse qPCR primers (*Tenascin-C*) 5′-AGG AGC TGG AGT TGC TGG TA-3′ 5′-TTA CAG TTC CCA GGG CAG TC-3′	Microsynth AG	N/A
Mouse qPCR primers (*Cox-2*) 5′-GAT GCT CTT CCG AGC TGT G-3′ 5′-TCA TAC ATT CCC CAC GGT TT-3′	Microsynth AG	N/A
Mouse qPCR primers (*Mmp11*) 5′-GCG AGG GGT ACC TTC TGA G-3′ 5′-GAT GGC CAC GAA GGA AGT AG-3′	Microsynth AG	N/A

(*Continued on next page*)

Continued

REAGENT or RESOURCE	SOURCE	IDENTIFIER
Mouse qPCR primers (*PAI-1*) 5′-CGC CTC CTC ATC CTG CCT AAG-3′ 5′-CTG TGC CGC TCT CGT TTA CC-3′	Microsynth AG	N/A
Human qPCR primers (*NQO1*) 5′-GTG ATA TTC CAG TTC CCC CTG C-3′ 5′-AAG CAC TGC CTT CTT ACT CCG G-3′	Microsynth AG	N/A
Human qPCR primers (*GAPDH*) 5′-AAG GTC GGA GTC AAC GGA TT-3′ 5′-CTC CTG GAA GAT GGT GAT GG-3′	Microsynth AG	N/A
ChIP qPCR primers (*Nqo1* ns) 5′-CAC AGT AAT GAA GCC CAG GT-3′ 5′-CCC TGA AAT GCT CAG GTC AT-3′	Microsynth AG	N/A
ChIP qPCR primers (*Nqo1* ARE) 5′-AGC AGA ACG CAG CAC GAA T-3′ 5′-CAC TCA GCC GTG GGA AGT-3′	Microsynth AG	N/A
ChIP qPCR primers (*PAI-1* ARE 1) 5′-GGG CAG TAA CCC AAG AGA AA-3′ 5′-AGC CAT CAC AGA GAA GCT ATG-3′	Microsynth AG	N/A
ChIP qPCR primers (*Angptl2* ARE 1) 5′-AGC TGC TCA AGT CCG TTA C-3′ 5′-CTG AAG GCT GAC GTT GCT-3′	Microsynth AG	N/A
ChIP qPCR primers (*Gpc1* ARE 1) 5′-CTG AGC TGA TGA AGG CTA GTT-3′ 5′-CTA CAT CCA TAC GCC CTT TCT-3′	Microsynth AG	N/A
Recombinant DNA		
pLenti CMVtight Puro DEST encoding caNRF2	Garstkiewicz et al., 2017	N/A
pLenti CMV rtTA3 Blast	Garstkiewicz et al., 2017	N/A
LentiCRISPRv2-KEAP1	Garstkiewicz et al., 2017	N/A
Software and Algorithms		
FACSDiva Software, version 6	BD Pharmingen	N/A
FlowJo software, version X	Tree Star Inc	N/A
Graph Pad Prism Software	GraphPad Software	N/A
MayQuant Software version 1.4.1.2 for peak detection	Cox and Mann, 2008	N/A
Ingenuity Pathway Analysis Software	Qiagen	N/A
ImagePro® Plus software	Media Cybernetics Inc	N/A

CONTACT FOR REAGENT AND RESOURCE SHARING

Further information and requests for resources and reagents should be directed to and will be fulfilled by the Lead Contact, Sabine Werner (sabine.werner@biol.ethz.ch).

EXPERIMENTAL MODEL AND SUBJECT DETAILS

Animals

Mice were housed and fed according to Swiss guidelines. Male Col1α2Cre mice in C57BL/6 background (Florin et al., 2004) were bred with female CMVcaNrf2 mice (FVB/N background) to generate fibroblast-specific caNrf2 mice. Only progeny of the F1 generation were used for experiments. Alternatively, male Col1α2Cre mice were bred with female $Nrf2^{flox/flox}$ mice (C57Bl/6 background), and progeny from the F3 generation were used for experiments. The breeding schemes are shown in Figures S7A and S7B. To generate triple transgenic mice containing either the PDGFRα-eGFP or the ARE hPAP transgene, Col1α2Cre hemizygous mice were first bred with PDGFRα-eGFP or ARE hPAP hemizygous mice to generate double transgenic progeny, which were then used for breeding with CMVcaNrf2 mice.

Animal experiments were approved by the local veterinary authorities (Kantonales Veterinäramt Zürich). Back skin tumorigenesis experiments were approved by the relevant committee of the Veterinary Direction, Greek Ministry of Rural Development and Food.

METHOD DETAILS

Genotyping

Animals were genotyped using DNA extracted from ear biopsies. DNA was amplified by PCR using KAPA2G FAST Genotyping Mix (Kapa Biosystems, Wilmington, MA) and visualized via gel electrophoresis.

Isolation and Culture of Primary Dermal Fibroblasts

Primary fibroblasts were isolated from mouse skin at P2.5 and human fibroblasts were isolated from foreskins obtained from the University Zürich Hospital. For both mouse and human fibroblasts, dermis was separated from epidermis by incubating with a 5% trypsin/EDTA solution for 1 h at 37°C and gently peeling away the epidermal layer. The dermis was then minced into small pieces and incubated with 2.5 ml of a collagenase type II solution (500 U/ml; Worthington Biochemical Corporation, Lakewood, NJ) for 1 h at 37°C with manual agitation every 15 min. The cell suspension was poured through a 100 μm cell strainer and the contents centrifuged at 1,200 r.p.m. for 5 min. The resulting cell pellet was re-suspended in 8 ml of fibroblast medium (DMEM (Sigma, Munich, Germany)/10% fetal bovine serum/penicillin/streptomycin) and plated onto two 6 cm dishes. Medium was changed the following day and cells were passaged prior to confluency. Absence of mycoplasma was confirmed by PCR using the PCR Mycoplasma Test Kit I/C (PromoKine, Heidelberg, Germany).

Histology and Immunohistochemistry

Tissue samples were fixed in 4% phosphate buffered formaldehyde solution for 24 h at room temperature (RT), processed and embedded in paraffin. Alternatively, tissue was immediately frozen in tissue freezing medium® (Leica Biosystems, Wetzlar, Germany). Formalin-fixed tissues were sectioned (7 μm) and stained using hematoxylin and eosin or using the Herovici procedure (Herovici, 1963). Visualization of GFP^+ cells was carried out using frozen sections, which were counterstained with Hoechst 33342 (Sigma). For immunohistochemistry/immunofluorescence staining, paraffin sections were dewaxed and rehydrated using a xylene/ethanol gradient followed by antigen retrieval using citrate buffer (pH 6.0) at 95°C for 1 h. For bright-field samples, a biotin-conjugated secondary antibody, the Vectastain ABC kit (Vector Laboratories, Burlingame, CA) and the DAB peroxidase substrate kit (Vector Laboratories) were used for visualization.

Cell Culture Experiments

Ctrl and caNrf2 fibroblasts were counted and seeded at equal densities for every passage. Fibroblasts used for experiments were at passage 2. A final concentration of 50 μM tBHQ was used. Cells were treated for up to 72 h and given fresh tBHQ solution every 24 h. SFN was used at a concentration of 5 μM and CDDO-Im at a concentration of 5 nM and cells were treated for 24 h. Additionally, SFN was used to simulate chronic Nrf2 activation at a concentration of 5 μM for 2 passages with fresh SFN-containing media given every 3 days. For detection of intracellular ROS, H2DCFDA (Invitrogen, Carlsbad, CA) was added to the media at a final concentration of 50 μM and cells were incubated for 1 h at 37°C and 5% CO_2. Afterwards, they were trypsinized, centrifuged, resuspended in 150 μl PBS and analysed by flow cytometry (505 - 535 nm). ROS detection using CellROX® Orange (Thermo Fisher, Waltham, MA) was performed according to the manufacturer's instructions and analysed by flow cytometry (ex/em 545 nm/565 nm).

SCC13 cells (Rheinwald and Beckett, 1981) were cultured in DMEM/10% FBS. Human primary fibroblasts were transduced with lentiviruses allowing doxycycline-induced expression of a human caNRF2 mutant (Garstkiewicz et al., 2017) or with lentiviral vectors based on the lentiCRISPRv2 plasmid (Addgene, Cambridge, MA) encoding an expression cassette for Cas9 and different sgRNAs targeting *KEAP1*. For induction of caNRF2 expression, cells were treated with 1 μg/ml doxycycline (Sigma) or vehicle. Doxycycline/vehicle was re-administered 3x a week and cells were grown for 3 weeks at which point they were stained using SA-β-gal.

To analyse the effect of fibroblast conditioned medium on keratinocytes, primary murine fibroblasts at passage 2 were first grown to 75% confluency at which point the media was changed to media containing FBS depleted of calcium. This was done in order to prevent keratinocyte differentiation, which occurs rapidly when cultured using high calcium media. Fibroblasts were cultured for an additional 24 h and media supernatant was filtered using a 0.45 μm filter. Conditioned media was then frozen at -20°C until use. Primary keratinocytes were isolated from mice at P2.5 as previously described (Telorack et al., 2016) and 24 h after isolation, media was changed to conditioned media and keratinocytes were cultured for an additional 24 h.

RNA Isolation and qRT-PCR

RNA was isolated from cultured cells using Trizol® according to the manufacturer's instructions (Cat# 15596, Life Technologies, Carlsbad, CA) and reverse transcribed using the iScript™ cDNA synthesis kit (Cat# 1708890, BioRad, Hercules, CA). Quantitative PCR was performed using LightCycler® 480 SYBR Green I Master reaction mix (Roche, Rotkreuz, Switzerland). Data was quantified using second derivative maximum analysis and gene expression represented as relative to the internal housekeeping gene, *Rps29.*

Wound Healing Experiments

An excisional wound model was used to study wound healing kinetics, including re-epithelialization and contraction (Chen et al., 2015). Mice at either 4 or 10 weeks of age were anesthetized by intraperitoneal injection of ketamine/xylazine (100 mg ketamine / 5-10 mg xylazine per kg body weight). After shaving, four 5 mm diameter full-thickness wounds were created using a biopsy punch,

two wounds on either side of the dorsal midline. Mice were allowed to heal for either 5 or 14 days at which point mice they sacrificed by CO_2 inhalation. Wounds were excised and processed for further analysis.

Flow-Cytometric Analysis of Immune Cells

A piece of skin measuring 5 mm x 25 mm was removed from unwounded back skin or from the mid back between the upper and lower wounds, at least 2 mm away from any adjacent wound. The two upper wounds were excised using a 5 mm biopsy punch. Wounds and unwounded skin were stored in ice-cold RPMI-1640 medium and immediately processed. All tissues were weighed prior to processing. Tissue samples were minced into small pieces followed by incubation in Mg^{2+}/Ca^{2+}-free PBS with 10 mM EGTA for 20 min at 37°C while shaking at 65 r.p.m. Samples were then washed using PBS and incubated in 2 ml of medium containing 1.3 WU/ml Liberase TL (Roche) for 1 h at 37°C while shaking at 65 r.p.m., followed by incubation in medium containing 1 U/ml Dispase II (Roche), 0.2 mg/ml DNase I and 7.5 mM $MgCl_2$. Next, 8 ml of ice-cold PBS containing 10 mM of EGTA was added to the tubes and pipetted vigorously up and down. The cell suspension was passed through a 30 μm cell strainer. Cells were centrifuged for 10 min at 350 x g and resuspended in PBS containing antibodies against different cell surface markers. After a 30 min incubation on ice, stained cells were analysed using the BD LSRII Fortessa with FACSDiva software (Version 6, BD Pharmingen, San Diego, CA). Fluorescence emission compensation was performed using compensation beads (BD Biosciences). Staining and gating controls included isotype control and fluorescence minus one (FMO) samples. Compensation adjustment, gating and data analysis were performed using FlowJo software (Version X, Tree Star Inc, Ashland, OR) and data were exported for further processing (Figure S3D).

Fluorescence-Activated Cell Sorting for RNA Isolation

Tissue was processed as described for flow cytometry using the following antibodies: CD140a-APC (1:200, BioLegend, San Diego, CA), CD31-PE (1:400, eBioscience, San Diego, CA), CD45-Pacific blue (1:400, BioLegend) and CD49f-biotin (1:200 BioLegend) with streptavidin-BV711 (1:200, BioLegend). Fibroblasts were defined as $CD140a^+$, $CD31^-$, $CD45^-$ cells. Immune cells were defined as $CD45^+$ cells, keratinocytes defined as $CD45^-$, $CD31^-$, $CD140a^-$ and $CD49f^+$ cells. Cells were sorted into PBS, centrifuged and resuspended in 1 ml Trizol® for RNA isolation.

Preparation of Fibroblast-Derived ECM

Fibroblast-derived ECM was obtained using primary dermal fibroblasts at passage 2. Fibroblasts were seeded at confluency into cell culture dishes and allowed to incubate in complete medium for 5 days at 37°C and 5% CO_2. Cells were then washed with PBS and incubated for 20 min at RT with 0.2 M ammonium hydroxide, which removes cells while leaving the ECM intact. After 20 min, ammonium hydroxide was removed and the ECM was washed with PBS. ECM-coated dishes wered stored at 4°C for up to two weeks. ECM used for *in vitro* experiments was first treated with DNase and then washed one more time with PBS prior to adding cells. For geodin-treated dishes, a solution of 50 μM geodin (Abcam, Cambridge, UK) was added to ECM-coated dishes and incubated at 37°C for 30 min. The geodin solution was removed and cells were added directly onto the geodin-treated ECM without washing. ECM used for proteomics analysis was harvested from the dish by adding ECM lysis buffer (80 mM Tris pH 6.8, 3% SDS and 5% 2-mercaptoethanol) after which ECM was scraped off using a cell scraper.

Collagen and Collagen Cross-Link Analysis

Analysis of collagen and of collagen cross-links was performed as reported previously (Brinckmann et al., 2005). Briefly, specimens were reduced by sodium borohydride (Sigma, 25 mg $NaBH_4$/ml in 0.05 M NaH_2PO_4/0.15 M NaCl pH 7.4, 1 h on ice, 1.5 h at RT), digested with high purity bacterial collagenase (C0773; Sigma, 50 U/ml, 37°C, 12 h) and hydrolyzed in 6 N HCl at 110°C for 24 h. The hydrolysates were precleared by solid phase extraction and analysed on an amino acid analyzer (Biochrome30, Biochrome, Cambridge, UK). Quantification was based on ninhydrin generated leucine equivalence factors (DHLNL, HLNL, and HP: 1.8; HHMD: 3.4). The nomenclature used in this paper refers to the reduced variants of difunctional intermediate cross-links (DHLNL, HLNL). The collagen and protein contents of the specimens were analysed in an aliquot of hydrolysed specimens of the soluble and the residual fraction after collagenase solubilization prior to solid phase extraction. Collagen content was calculated based on a content of 14 mg hydroxyproline in 100 mg collagen.

Immunocytochemistry/Immunofluorescence Analysis of Cultured Cells

Fibroblasts were fixed in 4% paraformaldehyde for 15 min at RT. For γH2AX staining, cells were fixed using ice-cold methanol for 10 min at -20°C. A blocking solution of 1% BSA was used for all staining protocols. After blocking, cells were incubated with primary antibody at 4°C overnight, followed by secondary antibody incubation for 30 min at RT.

BrdU Incorporation Assay

BrdU (Sigma) was added to the existing cell culture medium at a final concentration of 10 μM and cells were allowed to incubate for 1.5 h at 37°C and 5% CO_2. Afterwards, cells were washed with PBS and fixed using 4% paraformaldehyde for 15 min at RT. Cells were then permeabilized using 0.1% Triton-X in PBS followed by incubation with 2M HCl for 30 min. The HCl solution was removed and cells were incubated with boric buffer (100 mM boric acid, 75 mM NaCl, 25 mM sodium tetraborate, pH 8.5) for 5 min. Blocking was performed using 1% BSA for 10 min followed by incubation with a FITC-coupled anti-BrdU antibody (11202693001, Sigma) at 4°C overnight. Cells were counterstained using propidium iodide.

hPAP Staining

Formalin-fixed, paraffin embedded tissue sections were dewaxed and rehydrated using a xylene-ethanol gradient and washed twice with PBS. Tissue sections were then incubated in a solution of TMN buffer (50 mM Tris, 10 mM $MgCl_2$, 100 mM NaCl, pH 10) at 65°C for 15 min. Tissues were washed twice using ddH_2O and incubated for 5 min in staining solution (100 mM Tris, 100 mM NaCl, 5 mM $MgCl_2$) plus 5-bromo-4-chloro-3′-indolyphosphate (BCIP)/nitro-blue tetrazolium chloride (NBT) colour development substrate (Promega).

SA-β-Gal Staining

SA-β-gal staining on cultured fibroblasts was performed based on procedures previously described (Debacq-Chainiaux et al., 2009). Briefly, cells were washed with PBS, fixed for 5 min using a solution of 2% formaldehyde and 0.5% glutaraldehyde, washed twice with PBS and incubated in SA-β-gal staining solution (40 mM citric acid/Na-phosphate buffer at pH 6.0, 5 mM $K_4Fe(CN)_6$, 5 mM $K_3Fe(CN)_6$, 150 mM KCl, 2 mM $MgCl_2$, 1 mg/ml 5-bromo-4-chloro-3-indolyl–D-galactoside (X-gal)) for 24 h at 37°C. Staining solution was then removed, and cells were washed twice with PBS and counterstained using hematoxylin. Images were taken at 20x magnification. For tissue sections, freshly harvested tissue was embedded in tissue freezing medium. SA-β-gal staining was performed on 14 μm sections using a fixative of 1% formaldehyde for 1 min, a staining solution at pH 5.5 and incubation at 37°C for 48 h. All other staining procedures were performed as described above. Tissue sections were counterstained using Nuclear Fast Red (N3020, Sigma).

Chromatin Immunoprecipitation (ChIP)

Fibroblasts were grown to ~80 - 90% confluency in 14 cm culture dishes. Cross-linking was performed by incubating in a solution of 1% formaldehyde in PBS for 10 min at room temperature followed by quenching with glycine for 5 min. Cells were then removed from the dish using a cell scraper in the presence of 4-benzenesulfonyl fluoride hydrochloride (AEBSF) in PBS. The cell suspension was then added to a 15 ml tube and centrifuged at 1,200 r.p.m. for 5 min at 4°C. The cell pellet was re-suspended in 120 μl of cell lysis buffer (50 mM Tris (pH 8.0), 10 mM EDTA, 1% (wt/vol) SDS, protease inhibitor mix (cOmplete Mini, 11836170001, Roche), 1 mM AEBSF and 20 mM Na-butyrate), vortexed and incubated on ice for 5 min. DNA fragmentation was performed using a probe sonicator with cycles of 30 s with 30 s breaks in between (cycle 0.5, 30% power). Appropriate DNA fragmentation (100 - 500 bp) was confirmed using gel electrophoresis. The fragmented chromatin was then mixed with 800 μl of RIPA buffer (10 mM Tris (pH 7.5), 140 mM NaCl, 1 mM EDTA, 0.5 mM EGTA, 1% (vol/vol) Triton X-100, 0.1% (wt/vol) SDS and 0.1% (wt/vol) Na-deoxycholate, cOmplete Mini protease inhibitor mix, 1 mM AEBSF and 20 mM Na-butyrate) and centrifuged at 12,000 x g for 10 min. The supernatant was divided into 9 aliquots and used as input chromatin. The following antibodies were used for IP: anti-histone H3 (Abcam), anti-Nrf2 (Santa Cruz, Santa Cruz, CA, for endogenous and caNrf2), anti-Nrf2 (MyBioSource, San Diego, CA for endogenous Nrf2), anti-rabbit IgG (Millipore, Molsheim, France). Prior to incubation with chromatin, 3 μg of the appropriate antibody was incubated with Dynabeads Protein A/G (Thermo Fisher) diluted 1:10 in 100 μl of RIPA buffer at 4°C for 2 h while rotating. The antibody-bead complexes were then captured using a DynaMag™-2 magnet (Thermo Fisher), washed using RIPA buffer and incubated with 100 μl of previously prepared chromatin overnight at 4°C while rotating. The samples were magnetically captured, washed with RIPA buffer and resuspended in DNA elution buffer (20 mM Tris-HCl (pH 7.5), 5 mM EDTA and 50 mM NaCl, 20 mM Na-butyrate, 1% (wt/vol) SDS and 50 μg/ml proteinase K). Samples were incubated at 68°C for 2 h while shaking at 700 r.p.m., followed by magnetic capture and removal of the supernatant containing the DNA into a new tube. DNA was purified by phenol-chloroform phase separation and precipitated in a solution of 70% ethanol with 0.1 M sodium acetate and 15 μg of glycogen at -80°C for 2 h. After precipitation, DNA was centrifuged at 17,000 x g for 30 min at 4°C and the pellet washed with 70% ethanol. Finally, the pellet was resuspended in 50 μl of TE buffer (10 mM Tris-HCl (pH 8.0) and 10 mM EDTA) and heated at 95°C for 10 min. DNA was then analysed by qPCR for the presence of DNA fragments containing the ARE sequence of interest.

ECM Analysis by Mass Spectrometry

ECM isolates were concentrated by ultrafiltration using vivaspin columns (30 kDa MWCO). Samples were heated in SDS-PAGE loading buffer, reduced with 1 mM DTT for 10 min at 75°C and alkylated using 5.5 mM iodoacetamide for 10 min at RT. Protein mixtures were separated on 4-12% gradient gels (Nupage, Thermo Fisher). The gel lanes were cut into 5 equal slices, the proteins were in-gel digested with trypsin (Promega, Dübendorf, Switzerland), and the resulting peptide mixtures were processed on STAGE tips and analysed by LC-MS/MS (Rappsilber et al., 2007; Shevchenko et al., 2006).

Mass spectrometric (MS) measurements were performed on a QExactive Plus mass spectrometer (Thermo Scientific) coupled to an EasyLC 1000 nanoflow–HPLC. HPLC–column tips (fused silica) with 75 μm inner diameter were self-packed with Reprosil–Pur 120 C18-AQ, 1.9 μm (Dr. Maisch GmbH, Ammerbuch, Germany) to a length of 20 cm. Samples were applied directly onto the column without a pre–column. A gradient of A (0.1% formic acid in water) and B (0.1% formic acid in 80% acetonitrile in water) with increasing organic proportion was used for peptide separation (loading of sample with 0% B; separation ramp: from 5–30% B within 85 min). The flow rate was 250 nL/min and for sample application 600 nL/min. The mass spectrometer was operated in the data–dependent mode and switched automatically between MS (max. of $1x10^6$ ions) and MS/MS. Each MS scan was followed by a maximum of ten MS/MS scans using normalized collision energy of 25% and a target value of 1000. Parent ions with a charge state from z = 1 and unassigned

charge states were excluded for fragmentation. The mass range for MS was m/z = 370–1750. The resolution for MS was set to 70,000 and for MS/MS for 17,500. MS parameters were as follows: spray voltage 2.3 kV; no sheath and auxiliary gas flow; ion–transfer tube temperature 250°C.

Ear and Back Skin Tumorigenesis Assays

Tumorigenesis assays in mouse back skin were performed as previously described (Papadopoulou and Kletsas, 2011). Two intradermal injections (150 μl/injection) were performed at the back of each NOD/SCID mouse (n=8), one containing SCC13 cells (Rheinwald and Beckett, 1981) with ctrl mouse fibroblasts and one containing SCC13 cells with caNrf2 mouse fibroblasts. Each injection contained 10^6 SCC13 cells with an equal number of mouse fibroblasts. Approximately one month later, the animals were sacrificed, and the tumors were removed, used for weight determination and then fixed in 4% paraformaldehyde.

For ear tumorigenesis assays, 3 μl cell suspensions were injected intradermally into the ear of NOD/SCID mice (n=4). One ear contained ctrl fibroblasts/SCC13 cells and the other ear contained caNrf2 fibroblasts/SCC13 cells. 2 x 10^5 fibroblasts and 2 x 10^5 SCC13 cells were injected into each ear (4 x 10^5 cells total per injection). Tumor formation was monitored over 5 weeks at which point mice were sacrificed and tumors were harvested, used for weight determination and then fixed in 4% paraformaldehyde.

RNA Sequencing

Total RNA was isolated from crtl (n=3) and caNrf2 (n=3) fibroblasts using Trizol®. RNA quality was determined with a Qubit® (1.0) Fluorometer (Life Technologies) and a Bioanalyzer 2100 (Agilent Technologies, Santa Clara, CA). Only samples with a 260 nm/280 nm ratio between 1.8–2.1 and a 28S/18S ratio within 1.5–2 were further processed. The TruSeq RNA Sample Prep Kit v2 (Illumina, Inc., San Diego, CA) was used in the succeeding steps. Briefly, total RNA samples (100-1000 ng) were poly-A enriched and reverse-transcribed into double-stranded cDNA. cDNA samples were fragmented, end-repaired and polyadenylated before ligation of TruSeq adapters containing the index for multiplexing. Fragments containing TruSeq adapters on both ends were selectively enriched by PCR. The quality and quantity of the enriched libraries were validated using a Qubit® (1.0) Fluorometer and the Caliper GX LabChip® GX (Caliper Life Sciences, Inc., Waltham, MA). The libraries were normalized to 10nM in Tris-Cl 10 mM, pH8.5 with 0.1% Tween 20.

The TruSeq PE Cluster Kit HS4000 or TruSeq SR Cluster Kit HS4000 (Illumina, Inc) was used for cluster generation using 10 pM of pooled normalized libraries on the cBOT. Sequencing was performed on the Illumina HiSeq 2000 paired end at 2 x 101 bp or single end 100 bp using the TruSeq SBS Kit HS4000 (Illumina, Inc).

Quality control was performed on raw FASTQ files using FastQC (Babraham Bioinformatics) followed by alignment to the mouse genome (GRCm38) using STAR (Dobin et al., 2013). Reads were counted using RSEM (Li and Dewey, 2011) and differential expression and gene ontology enrichment analysis was generated using EdgeR software (Robinson et al., 2010).

QUANTIFICATION AND STATISTICAL ANALYSIS

Statistical Analysis

Statistical testing was performed using Graph Pad Prism (GraphPad Software, La Jolla, CA). Experiments used for statistics were repeated 2-5 times with all measurements taken from distinct samples (eg. separate wounds, animals etc.). Quantitative data are expressed as mean ± SEM. If not otherwise stated, significance was calculated with the Mann–Whitney U test; $^*P<0.05$, $^{**}P<0.01$, and $^{***}P<0.001$.

Histology and Wound Morphometry

Skin histomorphometry and wound healing kinetics were examined using hematoxylin- and eosin-stained sections. The parameters and methods used for analysis are summarized in Figures S7C and S7D.

Quantification of Histological Staining

All quantification was performed using ImagePro® Plus software (Media Cybernetics Inc., Rockville, MD). Ki67 positive epidermal cells during homeostasis and in the wound epidermis were quantified by counting the number of positively stained epidermal cells per micrometer of epidermis length. Images used for analysis were taken at 20x magnification. For quantification of SA-β-gal staining, 3-5 random images were taken at 20x magnification from wound granulation tissue. The area of granulation tissue was measured in mm^2 and the number of SA-β-gal positive cells within this area was counted. For quantification of tissue sections stained using the Herovici stain or PAI-1 immunohistochemistry, images were taken at 10x magnification and the colour of interest was set manually. For the Herovici stain, blue/purple pixels were considered positive and for PAI-1 immunohistochemistry, brown pixels were considered positive. The same colour segmentation settings were used for each image. For the Herovici stain, the number of positively stained pixels were expressed either as percent of total pixels (all colours not including background) within the wound bed or the absolute area of positively stained tissue per wound in mm^2. For PAI-1 immunohistochemistry, the number of positively stained pixels (brown) were expressed as a percentage of total pixels (all colours not including background) within the wound bed.

Quantification of Cytochemical Staining

Quantification was performed using the software ImagePro® Plus software (Media Cybernetics Inc., Rockville, MD). Quantification of SA-β-gal staining on cells was done using images taken at 20X magnification. A minimum of 10 random images were taken per sample and the number of SA-β-gal positive cells were counted and expressed as a percentage of total cells.

Quantification of Immunofluorescence Staining

All quantification was performed using ImagePro® Plus software (Media Cybernetics Inc.). For quantification of GFP positive fibroblasts during homeostasis, 3-4 random images were taken at 10x magnification. The area of dermis was measured, and the number of GFP positive cells was determined. For quantification of proliferating fibroblasts in wounds, images were again taken at 10x magnification and the area of granulation tissue was determined. Cells positive for both GFP and Ki67 were counted within the granulation tissue and expressed as the percentage of total GFP positive cells within the granulation tissue. Quantification of Meca32 positive staining was performed using images taken at 10x magnification, followed by determination of the granulation tissue area. Positively stained pixels were quantified automatically using images containing only the red (Meca32) channel, and data are expressed as percentage Meca32 positive pixels. For quantification of BrdU and γH2A.X positive cells, 5-6 random images were taken per sample at 10x magnification. Positively stained cells were counted and expressed as a percentage of total cells.

Ingenuity Pathway Analysis

Lists of differentially expressed genes from caNrf2 vs ctrl fibroblasts were uploaded to Ingenuity® Pathway Analysis (Qiagen, Hilden, Germany). Core analysis was performed with filtered lists of significantly up- or downregulated genes with a p-value of <0.05. The number of analysis-ready genes was 4574. Illustrations of the top enriched 'Canonical Pathways' with overlaying gene expression were exported. Data from the top 'Upstream Regulators' was exported. Data tables associated with 'Diseases & Functions' were exported to identify highly activated enriched functions in caNrf2 vs ctrl fibroblasts. Selected functions were arranged in a spreadsheet, and their activation z-scores were color-coded for visualization. Original IPA output data with unfiltered 'Canonical Pathways', 'Upstream Regulators' and 'Diseases & Functions' are provided in Table S1.

Gene Set Enrichment Analysis

Sets of significantly up- and downregulated genes were generated by re-analysing published microarray data from fibroblasts upon induction of senescence by bleomycin or by multiple passaging (replicative senescence) and from various cancer-associated fibroblasts; the datasets and samples analysed as well as methods for obtaining the gene sets are listed in Table S2. Original gene sets were uploaded to GSEA and filtered to those mapped by gene symbol present in the tested datasets. The gene sets were tested against the GSEA-generated ranked gene lists of the caNrf2 vs ctrl comparison as well as two other comparisons (bleomycin-induced senescence vs control fibroblasts and fibroblasts undergoing replicative senescence vs young fibroblasts from the Gene Expression Omnibus (GEO) accession GSE13330). GSEA was performed using the following settings:

Number of Permutations	5000
Permutation type	Gene Set
Enrichment statistic	Weighted
Metric for ranking genes	Signal2Noise
Gene list sorting mode	Real
Normalization mode	Meandiv
Randomization mode	No_balance
Omit features with no symbol match	True

Two separate GSEA runs were completed: 1) testing the caNrf2 vs ctrl fibroblast comparison against senescence-associated fibroblast gene sets consisting of up- and downregulated genes, and 2) testing the caNrf2 vs ctrl fibroblast comparison and two senescent vs non-senescent fibroblast comparisons (see above) against respective top upregulated gene sets, Nrf2 pathway genes, and Nrf2 Chip-seq data sets, and selected CAF gene expression profiles. GSEA results were organized in tables, and the normalized enrichment scores (NES) and FDR values were color-coded for visualization. Original and filtered gene sets, ranked gene lists, and original GSEA output data for all experiments are provided in Table S2.

Data Analysis of Matrix Proteomics Experiments

The MS raw data files were uploaded into the MaxQuant software version 1.4.1.2 for peak detection, generation of peak lists of mass error corrected peptides, and for database searches (Cox and Mann, 2008). A full-length UniProt mouse database additionally containing common contaminants such as keratins and enzymes used for in–gel digestion (based on UniProt mouse FASTA version April 2016) was used as reference. Carbamidomethylcysteine was set as fixed modification and protein amino–terminal acetylation and

oxidation of methionine were set as variable modifications. LFQ was chosen as quantitation mode. Three missed cleavages were allowed, enzyme specificity was trypsin/P, and the MS/MS tolerance was set to 20 ppm. The average mass precision of identified peptides was in general less than 1 ppm after recalibration. Peptide lists were further used by MaxQuant to identify and relatively quantify proteins using the following parameters: peptide and protein false discovery rates, based on a forward-reverse database, were set to 0.01, minimum peptide length was set to 7, minimum number of peptides for identification and quantitation of proteins was set to one which must be unique, minimum ratio count was set to two, and identified proteins were requantified. The 'match-between-run' option (2 min) was used.

The output ECM proteomics data was further filtered to those proteins, which exhibited >4 detected peptides and had absolute ratios of (average intensity + 0.1)>2. The gene symbols of these proteins were then compared with filtered lists of up- and downregulated genes from the RNA-seq data (FDR<0.05, $\log_2$fold>0.8 and <-0.5) and visualized by Venny 2.1.0 (http://bioinfogp.cnb.csic.es/tools/venny/index.html). Common genes were further analysed by Enrichr (Kuleshov et al., 2016), specifically by the ChEA and Wikipathways tabs.

DATA AND SOFTWARE AVAILABILITY

Data Deposition

RNA-seq datasets used in this publication have been deposited in NCBI's Gene Expression Omnibus (Edgar et al., 2002) and are accessible through GEO Series accession number GSE106097 (https://www.ncbi.nlm.nih.gov/geo/query/acc.cgi?acc=GSE106097). The mass spectrometry proteomics data have been deposited to the ProteomeXchange Consortium via the PRIDE (Vizcaino et al., 2016) partner repository with the dataset identifier PXD007999. Figures and Tables containing associated source data include Figures 3, 5, 6, 7, S1, and S4 and Tables S1, S2, S3, and S4. Upon publication, no restrictions have been placed on the availability of these data.